Agreement INGV-DPC 2007-2009

Project S 1: Analysis of the seismic potential in Italy for the evaluation of the seismic hazard

Responsibles: Salvatore Barba, Istituto Nazionale di Geofisica e Vulcanologia, and Carlo Doglioni, Università di Roma "La Sapienza"

http://groups.google.com/group/INGV-DPC-2007-S1
(restricted access)

Deliverable 1 # A3.13.1-2-3-4-5

Maximum Observable Shaking (MOS) maps of Italy (Final report)

10th June 2010

prepared by UR 3.13

Zonno Gaetano[1], Musacchio Gemma[1], Meroni Fabrizio[1], Basili Roberto[2], Imperatori Walter[3] and Mai P. Martin[3]*

[1] Istituto Nazionale di Geofisica e Vulcanologia, Sezione di Milano-Pavia, Milano

[2] Istituto Nazionale di Geofisica e Vulcanologia, Sezione di Roma 1, Roma

[3] Institute of Geophysic, ETH Zurich, Switzerland

(*) New affiliation (as of June 1, 2009) King Abdullah University of Science & Technology (KAUST), Division of Physical Sciences & Engineering (Thuwal, Saudi Arabia)

INDEX

1 Description of the Deliverable

The accurate prediction of intensity and variability of strong motions for future earthquakes greatly depends on our ability to simulate realistic rupture models for the near-field (NF), and realistic Earth structure for the far-field (FF).

The increasing number of recordings collected by dense, strong-motion networks irrefutably show the complexity of earthquake shaking, which is governed by a number of partially interacting physical processes. The variability of shaking intensity and the complexity of wave motion arise from three physical processes: (I) the complex dynamics of earthquake ruptures that radiate seismic waves; (II) the propagation of these seismic waves through the heterogeneous Earth; (III) the interaction of the seismic wavefield with the local geology/ morphology. Characterizing, quantifying, and modeling ground-motion complexity (by means of empirical scaling relations or by numerical simulations) requires investigation of these three physical processes. Regardless of the recent developments and scientific progress in the definition of earthquake sources and the complex medium through which seismic waves propagate, earthquake ground-motion observations are often at odds with standard prediction curves. On the other hand, the prediction of the ground motion arising from future earthquakes is crucial for earthquake engineers who are concerned about seismically safe design, and for seismologists who study the physical processes leading to ground-motion complexity.

In our studies, we investigate wave motion through numerical simulations that take into account primarily the ground acceleration in response to a given earthquake rupture that radiates seismic waves. The shaking that potential sources might cause is plotted on maps that provide a general overview of the hazard over a large area, and that can be used as the starting point for further detailed investigations. Here, we establish a procedure to compute ground motion that spans the entire frequency range of engineering interest (i.e., broad-band), and we derive the maximum shaking that is caused by expected earthquakes throughout Italy (i.e. the maximum observable shaking; MOS). Our approaches merge updated knowledge of the Italian regional tectonic setting and of source-zone definitions (Valensise and Pantosti, 2001; Basili et al., 2008) and scenario-like calculations of the expected MOS in any given area.

Figure 1 . Google map showing the individual seismic sources and seismic zones, from the DISS database (Basili et al., 2008).

For each source zone (Fig. 1) included in the Database of Italian Seismogenic Sources (DISS, Basili et al., 2008), deterministic low frequency near-field (LF: NF) waveforms need to be combined with high frequency far-field (HF: FF) stochastic synthetic seismograms to retrieve the hybrid broad-band wavefield. While considerable caution is taken to retrieve physics-based rupture source models, the Earth structure is derived from published data, and site effects are ignored.

In this report, we provide a step-by-step description of the general framework of the MOS computation, with an overview of the ideas that drove us during the project. At present, we provide the MOS map of Italy for the HF range. We have carried out broad-band analyses of the Messina 1908 earthquake, to test the work-flow for a given single site; we have computed broad-band maps around the fault of the Colfiorito 1997 earthquake, to test the entire work-flow that starts from a rupture model to retrieve the MOS that can be observed for both the NF and FF. Furthermore, we have derived and tested the algorithms that allow computation of the MOS in the space surrounding it, while floating the fault along the composite seismic sources (CSS). This was carried out for the Macro Region MR4 in the central-northern Apennines, where the HF MOS map was plotted.

This report ends by presenting the procedure and the results of the HF MOS map of Italy relating to the specific Deliverable 3: "High-Frequency Maximum Observable Shaking Map of Italy from Faults", a validation that compares the MOS results with historical felt intensities from the Italian DBMI04 macroseismic database. Furthermore, through specific tests, we discuss the "uncertainty and analysis of variability" in the context of the MOS procedure.

1.1 Definition of maximum observable shaking

We have used the DISS database and the maximum credible earthquake (MCE) to define the best representation of the MOS over the large areas that an active tectonic structure might be generated (Lorito et al., 2008). In the database, the active tectonic structures at the regional scale are embedded in seismic zones (SZs), where a number of individual fault segments are associated to a unique typical fault (TF) that can release its MCE and float along the entire SZ. We compute the MOS in terms of the peak ground acceleration (PGA), peak ground velocity (PGV), spectrum intensity/ Housner intensity (SI-HI), and displacement response spectra (SDs) caused by the MCE released within a SZ.

Since we aim at MOS computation for the entire range of seismic frequency, we had to derive both LF and HF waveforms from which we can compute ground displacement, velocity and acceleration. It is possible to compute ground motion for the entire frequency range typical of a seismic source only using the Green's function methods, such as the discrete wave-number/ finite element method of Olson et al. (1984). However, computation costs for complete Green's functions increase dramatically with increasing frequency, such that its applicability is usually limited to the LF ($f \leq 3$ Hz). For this reason, we chose to compute LF and HF waveforms separately, and then to merge them into the frequency domain following the approach suggested by Mai and Beroza (2003).

The general full procedure to evaluate the MOS is as summarized as below:

I. The MCEs of SZs (or composite sources) are derived from the DISS 3.0.4 database;

II. The credible rupture parameters. The rupture model is assessed by generating 30 realizations of stochastic slip distribution (Mai and Beroza 2002) and considering a constant, but moment-dependent, time rise and a rupture velocity. The source parameters are derived from the Mw using a standard scaling relationship, and compared with those included in the DISS database;

III. Computation of the LF wavefield at the site and for the MCE;

IV. Computation of the HF wavefield at the site and for the MCE;

V. Merging of the LF and HF wavefields in the frequency domain, to obtain the hybrid broad-band at the site and for the MCE;

VI. Extraction from the broad-band time series of some shaking parameters [i.e. PGA, PGV and/or SI-HI derived from the response spectral acceleration (5% damping) and the pseudo-velocity response spectrum (5% damping)];

VII. Steps III to VI are repeated for each point of a given grid surrounding the TF, to obtain a grid broad-band shake map associated to a MCE and a TF;

VIII. The MOS map. As the TF floats along the SZ, we allow the shake map to 'float' as well. At each point of the grid surrounding the SZ, we extract the maximum value from the computed shaking parameter.

While step (I) is taken from the DISS database, all of the other steps were computed entirely within the work-flow that we have completed.

1.1.1 Low-frequency ground motion

In the LF range (<3.5 Hz), a complete response of the Earth structure, including P-waves and S-waves, surface waves and NF terms, is computed from the Green's functions using the discrete wavenumber/ finite element method of Olson et al. (1984).

Mathematically, the time-dependent ground displacement uk(t) at a particular location k is described as:

$$u_k(t) = s(t) * g_k(t) * l_k(t)$$

where * is the convolution operator, s(t) is the source effect due to the earthquake rupture, $g_k(t)$ describes the path effects due to wave propagation from source to site k, and $l_k(t)$ describes the local site effects due to small-scale geological conditions for the k observation point. This equation quantifies the ground.motion generation, omitting for simplicity an additional instrument response that modulates the seismic recording. The earthquake-source contribution can be further subdivided into effects the originate from the local time-dependent particle motion on the fault, p_{ij}, and from the rupture finiteness, f(t). The term $g_k(t)$ is the Earth transfer function, and it contains contributions from the layered Earth structure and seismic-wave attenuation, although it can also comprise effects due to random heterogeneities in the Earth and/or basin and topographic structures. The Earth is defined in a three-dimensional (3D) Cartesian space, as a 1D function of depth (z), and with a free surface at z=0. In our computation, the factor lk(t) is not considered. At this stage, the anaelastic attenuation is not included, as the effects on the 0-2 Hz frequency range are negligible.

The computation time increases with frequency, size of fault, and number of observation points. To allow the best compromise between computation costs and output, we had to limit the LF wavefield to 3.5 Hz and the fault size to 75 km. Only four traction surfaces were computed: for a dip of 75° for strike-slip faults; while 25°, 45° and 75° dips were used for normal and reverse faults.

1.1.2 High-frequency ground motion

The HF wavefield was computed through a finite-fault stochastic method and using the EXSIM_Beta code (Gail et al., 2009), a revised and simplified version of EXSIM_DMB (Boore, 2009) that in turn was derived from the EXSIM code, by Motazedian and Atkinson (2005). Moreover, we note that this EXSIM code was modified from the original early FINSIM code (Beresnev and Atkinson, 1998).

In this report, we refer to EXSIM_Beta (Gail et al., 2009) using only the name EXSIM. The fault plane was assumed to be a rectangle broken into an appropriate number of sub-faults, which are modeled as point sources using the approach of Boore (2003). The sub-faults radiate ω^2 spectra, and their sizes define their moment and corner frequency, while the number of triggered sub-faults is adjusted to reach a specified target moment (Mw).

The finite-fault model parameters require specification of: (1) the fault-plane geometry (e.g. length, width, orientation); (2) the source (e.g. slip distribution, stress drop, nucleation point, rupture velocity); and (3) the crustal properties of the region (e.g. geometric spreading coefficient, quality factor Q(f)). The different versions of the EXSIM finite-fault stochastic simulation program have been used extensively by the scientific community for purposes similar to those of the present study (e.g. Zonno et al., 2008). We have also slightly customized the code, to output the time series of acceleration and velocity corresponding to the mean on a set of stochastic realizations. Table 1 gives the input simulation parameters used with the EXSIM program.

Table 1. Input parameters of the stochastic EXSIM program

Parameter	Value
Moment magnitude (Mw)	5.9, 6.3, 6.7 and 7.1
Fault orientation (Strike)	0°
Fault orientation (Dip)	25°, 45° and 75°
Fault depth to upper edge (H)	1, 5 and 10 km
Fault dimension	Appendix 1.
Sub-fault length and width	Appendix 1.
Style of fault and rake	Appendix 1.
Input hypo at sub-fault	Appendix 1.
Fast fourier transform	Dynamic allocation of points
Sample interval	0.01 s
Shear-wave velocity	3.5 km/s
Density	2.694 gr/cm^3
Rupture velocity	0.8× shear-wave velocity
K	0.03 s
Q(f)	100.* f
Stress parameters	200 bars
Flocut, nslope	0.0 and 8
Iseed, nsims	309 and 30 runs
Geometric attenuation	If R < 30, R^{-1} ; or $R^{-0.5}$
Distance-dependent duration	To + 0.1 R (s)
Windowing function	Saragoni-Hart
Amplification function	Not applied
Slip model	Random & Gaussian distribution
Dynamic flag and pulsing (%)	1 and 50
Low frequency treatment	D_Motazedian's Taper
D_Motazedian's taper coeff	-0.50
Damping	5% critical damping

1.1.3 Broad-band ground motion

The broad-band wavefield computation follows a merging approach of the separately computed LF and HF seismic waves suggested by Mai and Olsen (2005) and Mena et al (2009), and recently modified by Imperatori and Mai (2009). Here, we have computed the LF wavefield deterministically, while the HF wavefield is derived with a finite-fault stochastic approach (see paragraph 1.1.3).

The amplitude spectra of the seismograms calculated according to the two techniques are reconciled at intermediate frequencies where their domain of validity overlaps (Mai and Beroza, 2003), as the composition of the hybrid broad-band seismograms is most effective in the frequency domain The combination of these two pre-computed waveforms results in much lower computation costs, while allowing for complete broad-band wave forms to derive ground-motion parameters. The resulting composite broad-band seismograms reflect the source complexity even at short-scale lengths, i.e. they capture the short-range variability of earthquake source models.

The current implementation of the methodology is carried out for the merge of LF deterministically computed waveforms with HF stochastic-computed waveforms with the EXSIM software. Due to intrinsic differences between the deterministic approach at LF and the stochastic approach at HF, minor timing differences occur, which we account for using cross-correlation. As LF and HF seismograms are computed for the same source model, their phase spectra are virtually

identical, and no significant phase mismatches occur. This method can account for arbitrarily complex earthquake rupture models, both at LF and HF. However, for a particular scenario earthquake on a given fault, multiple rupture-model realizations and stochastic HF wavefields need to be computed to capture the range and variability of the ground motion.

1.1.4 The earthquake source complexity

In our work-flow, MOS are computed by taking into account source complexity, and specifically the kinematics of the rupture, without considering the forces and stresses that cause these motions on the fault. In the present study, we used three major types of slip distribution, for which we derive rupture models to be used for both LF and HF wavefield computations: random, Gaussian, and stochastic. The stochastic approach is fully described in Mai and Beroza (2002). Strike, dip, rake and Mw are provided by the DISS database.

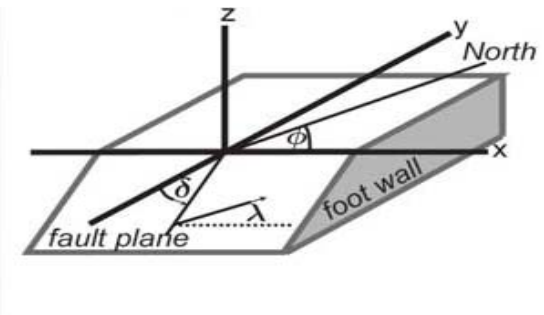

Figure 2. Geometrical definition of a fault.

The earthquake nucleates at the hypocenter, and it propagates over the fault plane with an average rupture velocity, which can show local variations due to initial stress conditions and the frictional properties on the fault. These conditions also determine the individual slip-time history for all points on the fault (which start sliding once they are reached by the propagating rupture front). As a first order, the shape of the local slip-velocity function depends on the overall fault dimensions (i.e. the fault aspect ratio), and the relative position of each point with respect to the rupture nucleation point and its distance to the closest fault edge.

We can generate extended-source stochastic rupture models based on random-field models for complex earthquake slip, with moment-dependent correlation lengths (Mai & Beroza, 2002). While the slip varies over the rupture plane, the rise time and rupture velocity are kept constant. Slip distributions obey the statistical properties and empirical laws that are based on physical principles. Although the source dimensions are those included within the DISS database, we run validation tests based on several scaling relationships (see Mai and Beroza, 2000, for details).

The stochastic distribution of slip on a fault plane is generated using a Von Karman correlation function with correlation lengths, a_x and a_y, scaling with the seismic moment (Mai and Beroza, 2002) and chosen to be at least about 1/3 of the fault dimensions. The hypocenter locations are generally assumed to be in the middle of the fault (bilateral rupture). However, simple assumptions on the distance to the asperities and on the possibility of generating a large earthquake are used to set the hypocenter location (Mai et al 2005).

1.1.5 The Earth structure

As detailed analyses of the Earth structure are beyond the scope of this study, we used crustal parameters from published data (Fig. 3) or interacted with a specific Research Unit (UR 2.02) in the framework of the S1 project. Although the code used for the LF waveforms allows detailed 1D velocity- and density-depth functions, the HF stochastic code requires only one average input velocity and density value.

As well as geometric spreading, the attenuation mostly related to anaelastic energy dissipation is accounted for only when computing the stochastic HF wavefield, since the LF code does not allow for attenuation as a function of frequency. On the other hand, we are confident in a first order of the approximation of our results, since attenuation becomes significant at HFs.

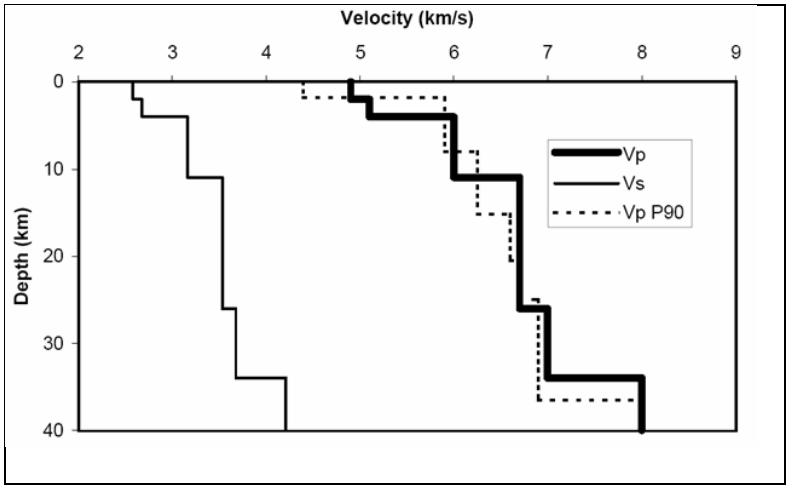

Figure 3. Velocity model (Ponziani et al, 1990) used to compute broad-band waveforms in the MR4 macro-Region (redrawn from Barba and Basili, 2000).

1.2 Broad-band applications at different scales

As the major goal of the project is to establish the work-flow for MOS map computation, we test the work-flow for the MOS maps at different scales and using different types of seismogenic sources included in the DISS database. The individual single sources are used to perform single site analyses and to test the merging of the LF-deterministic and HF-stochastic synthetic waveforms. The SZs are used to establish a procedure to compute the MOS for an entire macro-Region.

1.2.1 Single-site analyses: ground motion caused by the 1908 Messina earthquake

We studied the ground motion caused by the 1908 Messina earthquake for the individual single seismic sources included in the DISS database. The LF and HF motions were computed at a near-field site (Orti Superiore) and used to retrieve the hybrid broad-band waveforms. The details of this have been presented at different meetings, such as the Reggio Calabria meeting: *"1908-2008: cento anni dopo il grande terremoto"* and the *AGU Meeting 2008* (Zonno et. al., 2008). http://hdl.handle.net/2122/4742

1.2.1.1 Rupture models

We computed the LF and HF waveforms to investigate the ground-motion variability caused by different slip distributions (Fig. 4). Rupture simulations from 16 models (4 slip maps with 4 different hypocenter locations) were derived from 30 stochastic slip distributions of a left-lateral, strike-slip faulting mechanism.

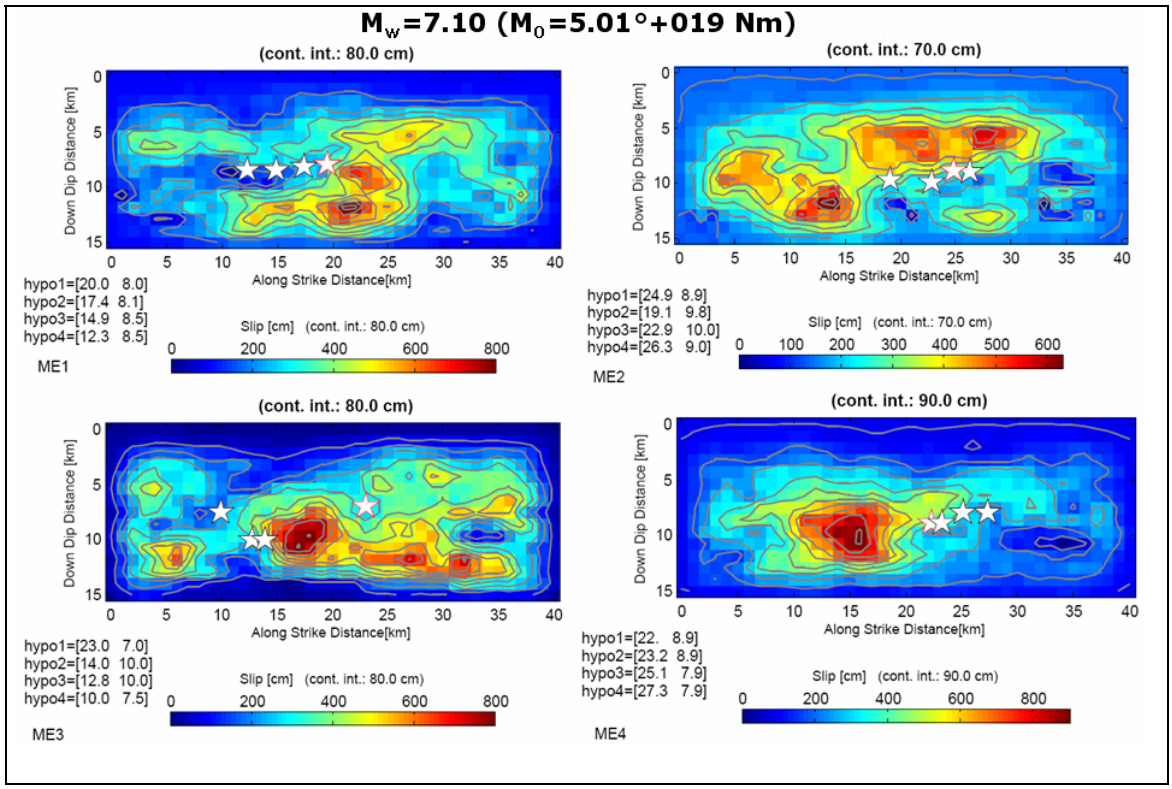

Figure 4. Rupture model for the Messina1908 Mw 7.1 earthquake. The rectangular box represents the width and length of the fault (W, 40 km, and L, 15 km). The slip distribution on the fault is color-coded and was derived following (Mai and Beroza 2002). The stars show the hypocenter locations. Figure taken from Zonno et al., (2008).

1.2.1.2 Broad-band simulation

We computed the hybrid motions for the four source models at a single site, using a matching frequency of 0.4 Hz. Figure 5 shows the case for the rupture model ME3.

The Fourier amplitude spectra of the simulated acceleration and velocity times series show the smooth transition between the deterministic LF contributions and the stochastic HF wavefield (Fig. 4). The validity of our approach is also demonstrated in the comparison of spectral acceleration in which the PSA (curve blue), from broadband time series, and fully captures the nature of the PSA due to the LF wavefield (red broken line) and the HF wavefield (green line). As such, our method is also useful to examine the relative influence of NF and FF effects on ground motion (see Deliverable 2 # A3.13.8 “Delimitation of near-fields boundaries”).

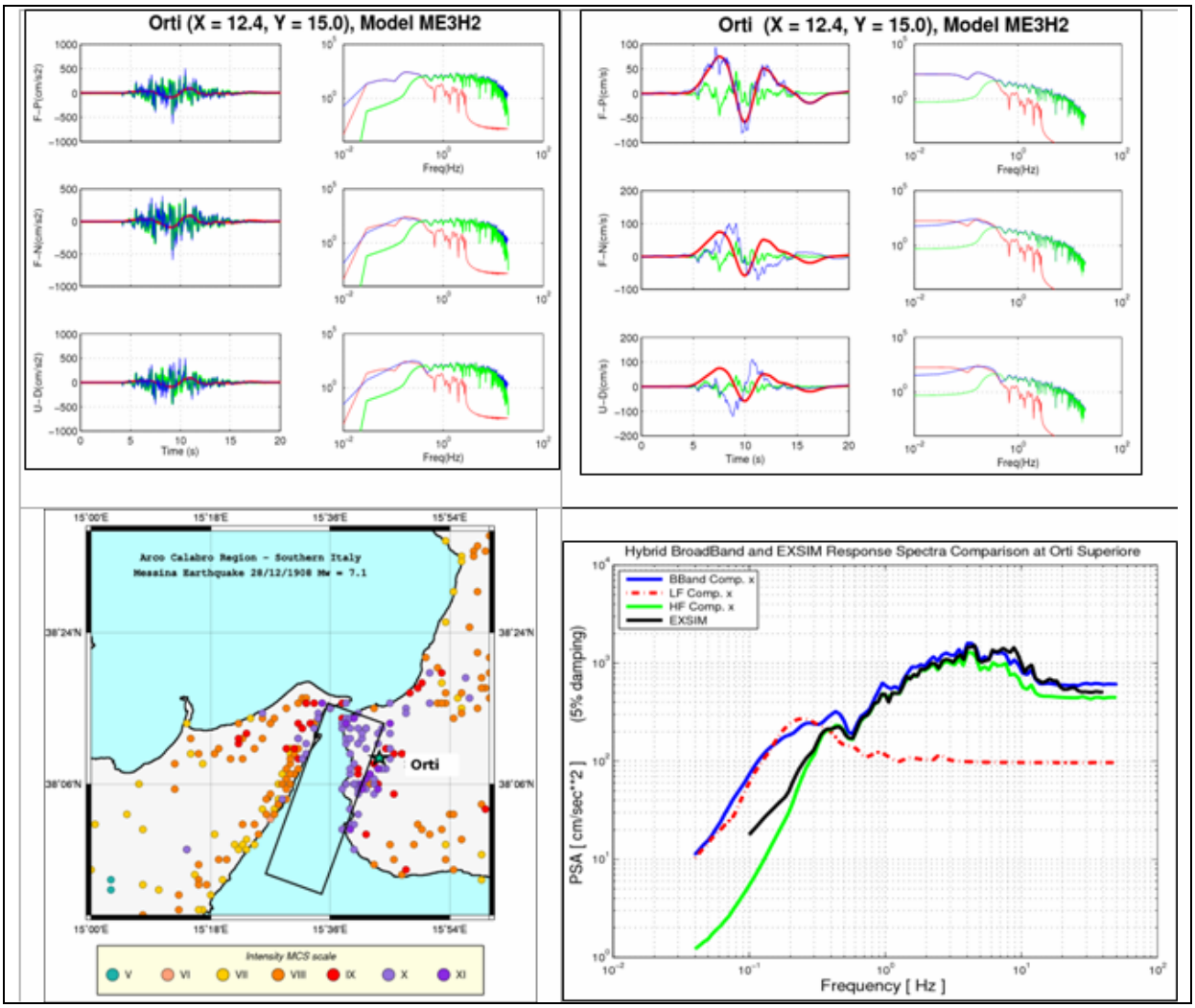

Figure 5. The response spectra acceleration are computed at Orti Superiore (green star on map). Top panels: acceleration (left) and velocity (right) waveforms in the time and frequency domains. Bottom panels: color-coded observed MCS intensities map (left) (DBMI04 , Stucchi et al., 2007), and spectral accelerations (5 % damping) (right). Figure taken from Zonno et al., 2008.

1.2.2 Regional-scale grid analysis

At the regional scale, we tested the procedures to compute the HF MOS map for a large area of the macro-Region MR4 (Fig. 6), which includes the central-northern Apennines extensional structures and some of the most relevant recent earthquakes in Italy (i.e., Avezzano 1915, Colfiorito 1997, and L'Aquila 2009). Here the active tectonic structures on a regional scale are merged into eight SZs, where the individual fault segments that are capable of releasing intermediate to large sized earthquakes (5.5 ≤Mw ≤6.7) range from between 2 and 29 (Table 1).

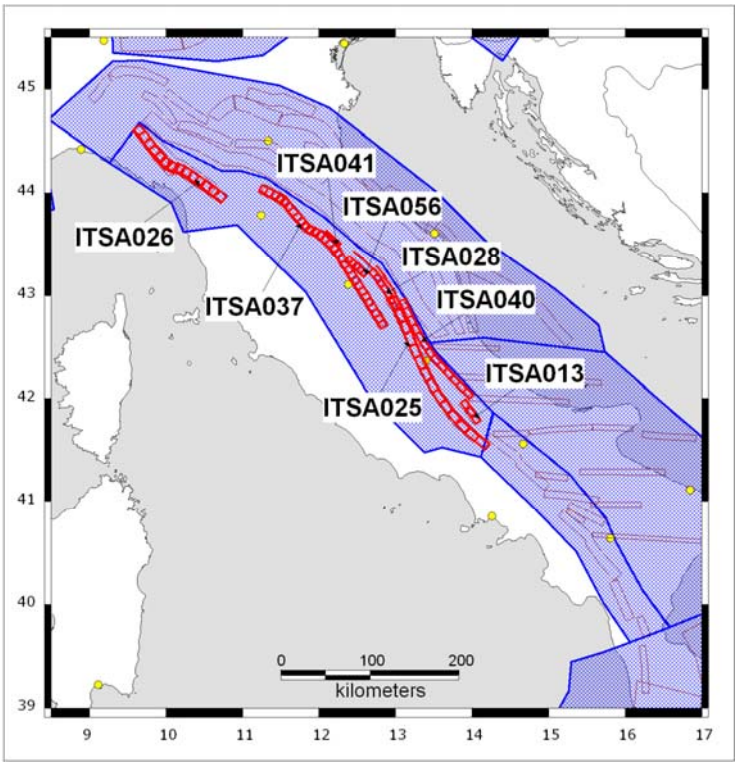

Figure 6. Macro-Region MR4 and its SZs (red lines): ITSA026, ITSA037, ITSA041, ITSA056, ITSA028, ITSA040, ITSA025 and ITSA013

Table 2. Summary of SZs included in macro-Region MR4. Details of the MCEs of the composite sources, from the DISS 3.04 database, are listed in Appendix 1.

# series	# TF	DISS code	Name of the SZ	Mw	Depth (km)
101 - 111	11	ITSA026	Lunigiana-Garfagnana	6.3	1.0
201 - 229	29	ITSA037	Mugello-Sansepolcro-Trevi	6.1	0.6
301 - 304	4	ITSA041	Selci-Lama	5.5	1.0
401 - 404	4	ITSA056	Gubbio Basin	6.0	2.5
501 - 506	6	ITSA028	Colfiorito-Sellano	6.0	3.4
601 - 612	12	ITSA040	Castelluccio-Sulmona	6.4	1.0
701 - 711	11	ITSA025	Norcia-Ovindoli-Barrea	6.7	1.0
801 - 802	2	ITSA013	Aremogna-Cinquemiglia	6.4	1.0

The HF MOS map for the entire macro-Region MR4 (Table 2) was presented in a meeting on 1-3 April, 2009, in Rome, before the L'Aquila earthquake of 6 April, 2009. The details will not be presented here because the floating-fault prototype algorithm is no longer used in the computation of HF MOS maps for the whole of Italy. Some of the details can be found in the poster presented http://hdl.handle.net/2122/5209

1.2.2.1 The Colfiorito 1997 earthquake

Here, we discuss the full procedure as applied to the Colfiorito 1997 earthquake (ITSA028), to evaluate the broad-band map on a grid around the fault. Afterwards, we allow the fault to float along the ITSA028 SZ, which includes six segments, to produce the MOS map. The Colfiorito 1997 earthquake has a MCE of moment magnitude Mw 6.0 and the TF was a dip-slip normal fault (rake, 275) striking 139° and dipping 40° with L = 14 km, W = 8 km, and the top at 3.4 km in depth.

Although source size was derived directly from the DISS database, we tested the source dimension against different scaling relationships, such as those of Wells and Coppersmith (1994) and Mai and Beroza (2000), to validate DISS input parameters. With the MCE representing the

Colfiorito 1997 earthquake all being similar (Table 3), we did not need any readjustment to the input parameters taken from the DISS.

Table 3. Rupture parameters for the $\mathbf{M}_w$ 6.0 MCE of the Colfiorito 1997 earthquake. In the bottom row, there are the rupture parameters readjusted by the rupture-generator code SlipReal for implementing earthquake source-scaling by Mai and Beroza (2000).

Input parameters for stochastic rupture simulation

	Rupture parameters									**Correlation function** (anisotropic von Karman ACF)		
	M_w	**L** *(km)*	**W** *(km)*	**mech**	**D_{mean}** *(cm)*	**D_{Max}** *(cm)*	**M_0** *(N m)*	**τ_r** *(s)*	**v_r**	**a_x** *(km)*	**a_y** *(km)*	**H**
DISS	6.0	14	8	ds	33		1.11e+018					
SlipReal	6.0	14	8	ds	30.36	152.5	1.12e+018	1.5	0.8	3	5	0.6

L, length; **W**, width; **mech,** faulting mechanism; $\mathbf{D}_{mean}$ and $\mathbf{D}_{Max}$, slip; $\mathbf{M}_o$, moment magnitude; $\boldsymbol{\tau}_r$, rise time; $\mathbf{v}_r$, rupture velocity ratio; $\mathbf{a}_x$, $\mathbf{a}_y$, **H,** correlation lengths and Hurst exponent of the von Karman correlation function.

The rupture model (Fig. 7) was derived from 60 stochastic realizations of slip maps (Mai and Beroza, 2002) on the fault dimensions and correlation functions (von Karman) listed in Table 3. The hypocenter location was chosen according to Mai et al, (2005) who find that ruptures tend to nucleate close to large-slip patches but not right on the largest-slip patch.

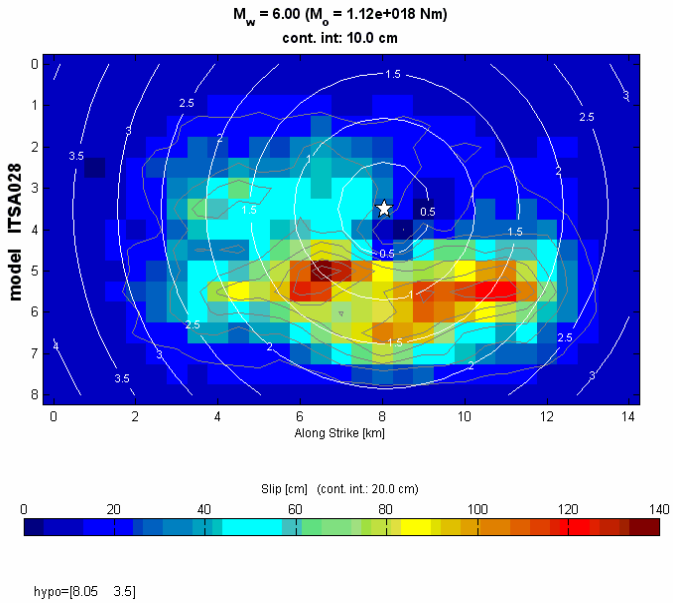

Figure 7. Rupture model for the ITSA028 MCE, simulated using the approach of Mai and Beroza (2002).

The LF (0-3 Hz) seismograms (velocity) were derived from convolution between the rupture model in Figure 6 and the tractions computed for the 1D Earth structure shown in Figure 3. The Green's functions were computed up to 3.5 Hz with a time step length of 0.0125 s (Table 4), for a total seismogram length of 80 s. Tractions were defined on a fault surface of 46 km length and up to 18 km depth, with a 40° dip and for 230 equally spaced receivers.

The HF (0.1-20 Hz) seismograms (velocity) were derived after 30 stochastic simulations. The seismogram that shows acceleration closest to the mean PGA among the 30 stochastic realizations was integrated to derive the HF velocity time series that is to be combined with the LF series.

Table 4. Input parameters for LF waveform computation using COMPSYN. For details concerning the significance of each parameter, see Spudich and Archuleta (1987) and Spudich and Xu (2003).

INPUT PARAMETERS FOR LOW FREQUENCY SYNTHETICS (COMPSYN)

Green's functions input parameters

F_{max} (Hz)	F_{cut} (Hz)	t_{max} (s)	dt (s)	T_{fde} (s)	R_{max} (km)	n_{k1}	n_{k2}	k_{sk}	$z_{min,\ max}$ (km)	z_{inc}	Comp
3.5	3.5	80.0	0.0125	8.0	360	1	2000	1	0.2, 20.0	1	B

Traction input parameters

F_{min} (Hz)	F_{int} (Hz)	F_{max} (Hz)	u_{min}, u_{max} (km)	v_{min}, v_{max} (km)	dip deg	dk	du_{min}	dv_{min}	m
0.0	3.0	3.5	-23.0, 23.0	0.5, 18.0	40	10.0	120.0	60	0.8

Slip input parameters

F_{min} (Hz)	F_{int} (Hz)	F_{max} (Hz)	m	Slip funct.	$u_{min,max}$ (km)	$v_{min,max}$ (km)	V_r/V_S	x_{obs}	y_{obs}	rnpw	nu_{min}	nu_{max}	durfr	rton	Xmomnt (dyne/cm)
0.0	3.5	3.5	0.8	B	-6.9, 6.9	3.41, 11.39	1	0	0	10.0	30.0	30.0	1.0	1.0	1.12e+025

1.2.2.2 Broad-band map on a grid around the Colfiorito 1997 fault

The LF and HF amplitude spectra were than reconciled at intermediate frequencies to derive the broad-band time series. We can see in Figure 8 that the circular-fault-centered shaking pattern typical of a simple HF computation is replaced by a more complex distribution, where high values of shaking occur both on the fault and in the lobe-shaped areas surrounding it (south-western corner on the map).

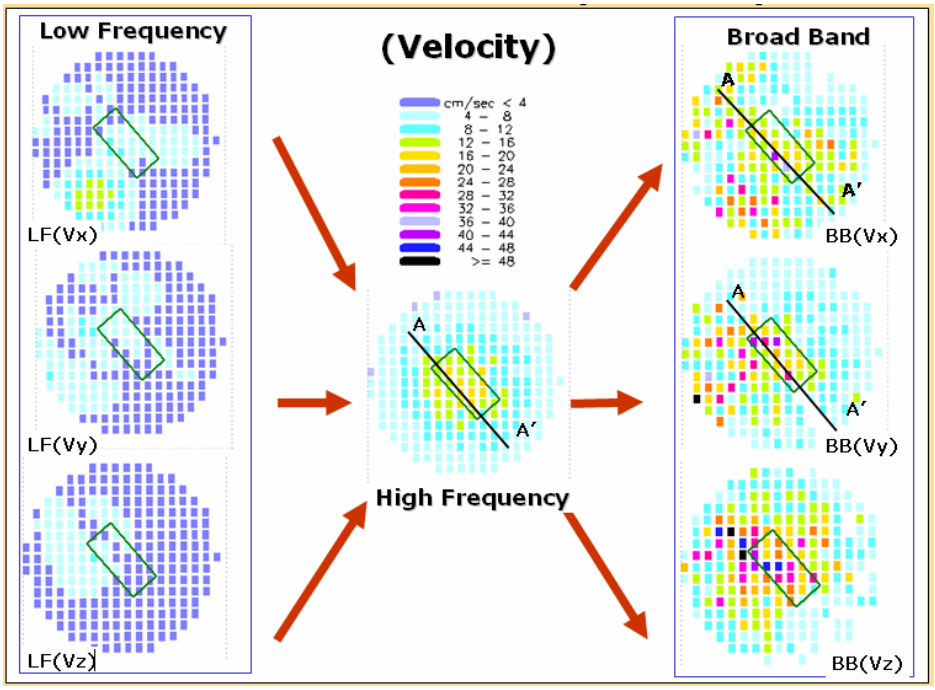

Figure 8. The maximum of the LF velocity time series (three components, in the left column), the maximum of HF velocity time series (in the middle column), and the maximum of the broad-band velocity time series on a grid surrounding the Colfiorito fault (right column). The LF and HF amplitude spectra were then reconciled at intermediate frequencies to derive the broadband time series.

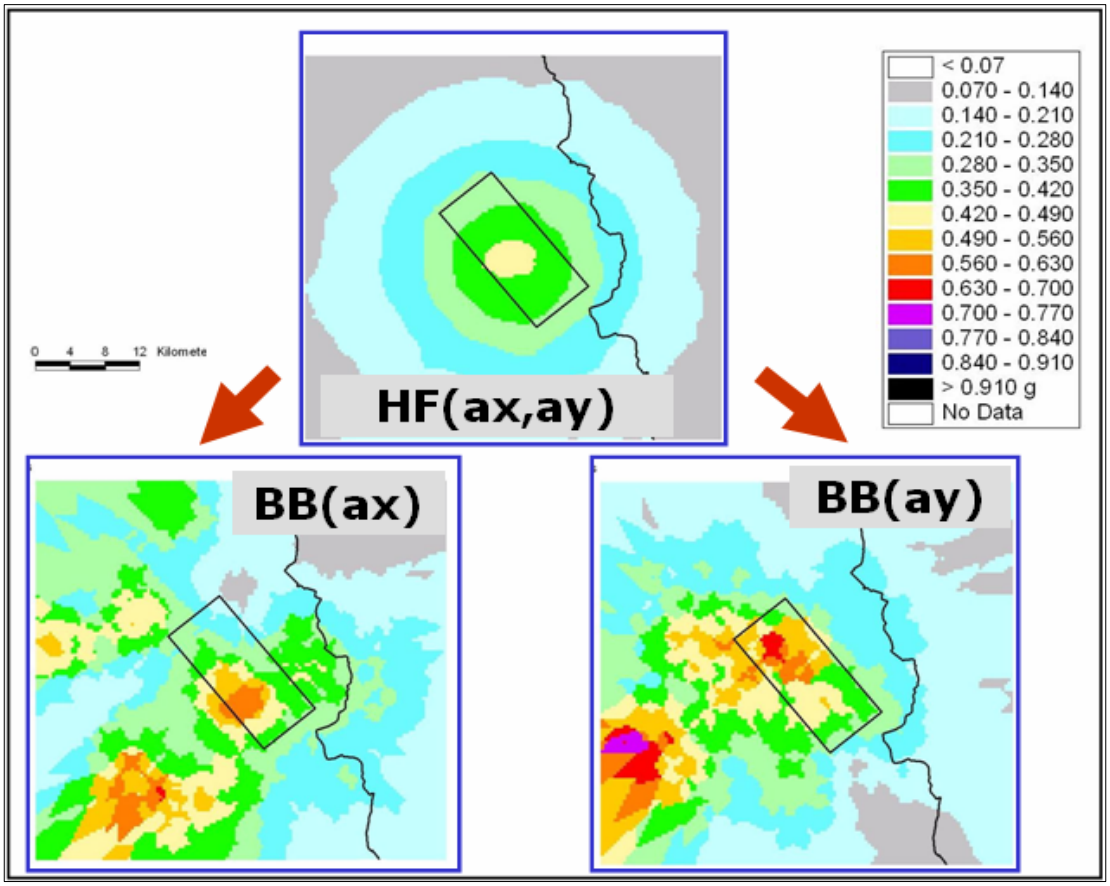

Figure 9. Comparison between HF- and broad-band-derived PGA maps for the TF (black box) and MCE of the Colfiorito 1997 earthquake. From top to bottom (and left to right) color coded PGA (g) maps are plotted for the HF, broad-band fault parallel and broad-band fault normal horizontal components.

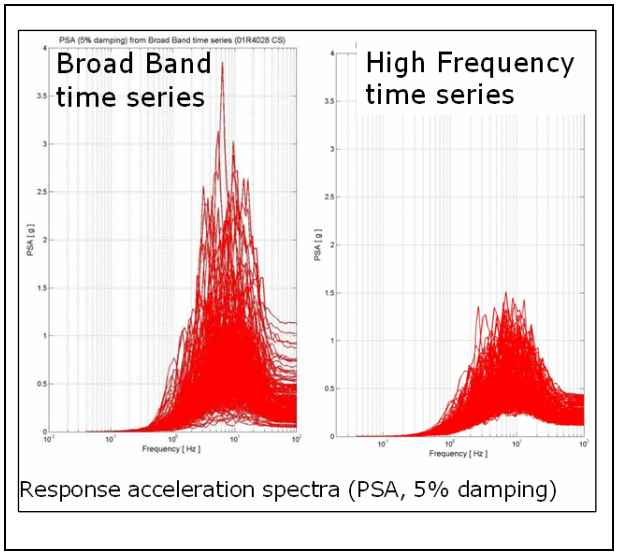

Figure 10 Comparison of response acceleration spectra (PSA, 5% damping) obtained from broad-band time series (left) and HF time series (right).

When taking into account the broad-band frequency content (from LF to HF), ground shaking reveals the complexity of the rupture process (Figs. 9 and 10). However, because the process of merging deterministic LF with stochastic HF waveforms is not a trivial task, several parameters needed to be tuned up. For instance, we have checked carefully the use of magnitude-dependent

constant rise time and the BBtool matching frequencies. The broad-band ground-shaking map might have spurious spots that can be avoided by applying smoothing to the plotting routine. We decided to apply only the HF MOS map procedure to the whole of Italy.

1.3 HF MOS map computation

Recent new and updated data about known seismogenic faults in Italy (Fig. 1) have been published (DISS Working Group, 2009), and this is the basic starting point of the MOS procedure. We can find the MCE as defined for each CSS and related TF for each part of Italy (Fig. 2). We grouped the TFs of the CSS according to the moment magnitude and the faulting mechanisms. Then we defined the credible rupture parameters, because the MCE is modeled as a rectangular fault plane (i.e. the TF). A finite-fault stochastic simulation generates the ground shaking around the TF in terms of the PGA, PGV, SI-HI and SDs.

Typical-fault derivation

Each TF inherits the geometric parameters of its parent CSS according to the following scheme (see Table 5):

a) Strike: local strike of the parent CSS following the map trace;
b) Dip: average value of dip angle values of the parent CSS;
c) Rake: average value of rake angle values of the parent CSS.

Table 5. Fault type classification

Rake (°)	*Fault type*
225 - 315	*Normal dip slip*
45 - 135	*Reverse dip slip*
135 – 225	*Right-lateral strike slip*
< 45 or > 315	*Left-lateral strike slip*

Moment magnitude

The size of the TF was derived from the maximum magnitude value (the MCE) of the parent CSS. For each TF, length (L) and width (W) was computed from the empirical relationships of Wells and Coppersmith (1994), according to the moment magnitude and fault type as given above:

$$\log_{10}(L \mid W) = a + bM_w$$

where L is the length and W is the width of the fault after Wells and Coppersmith (1994), while a and b depend on fault types, as shown in Table 6.

Table 6. The empirical relationships according to Wells and Coppersmith (1994)

Fault type	*Length=RLD*		*Width=RW*	
	a	***b***	***a***	***b***
Normal	*-1.88*	*0.50*	*-1.14*	*0.35*
Reverse	*-2.42*	*0.58*	*-1.61*	*0.41*
Strike slip	*-2.57*	*0.62*	*-0.76*	*0.27*

The average displacement was then obtained from the relationship:

$$\overline{D} = \frac{M_0}{\mu LW}$$

where μ is rigidity, L and W are length and width, respectively, and M_0 is the seismic moment equivalent to the MCE, as given by:

$$\log_{10} M_0 = 1.5M_w + 9.1$$

(Kanamori and Brodsky, 2004).

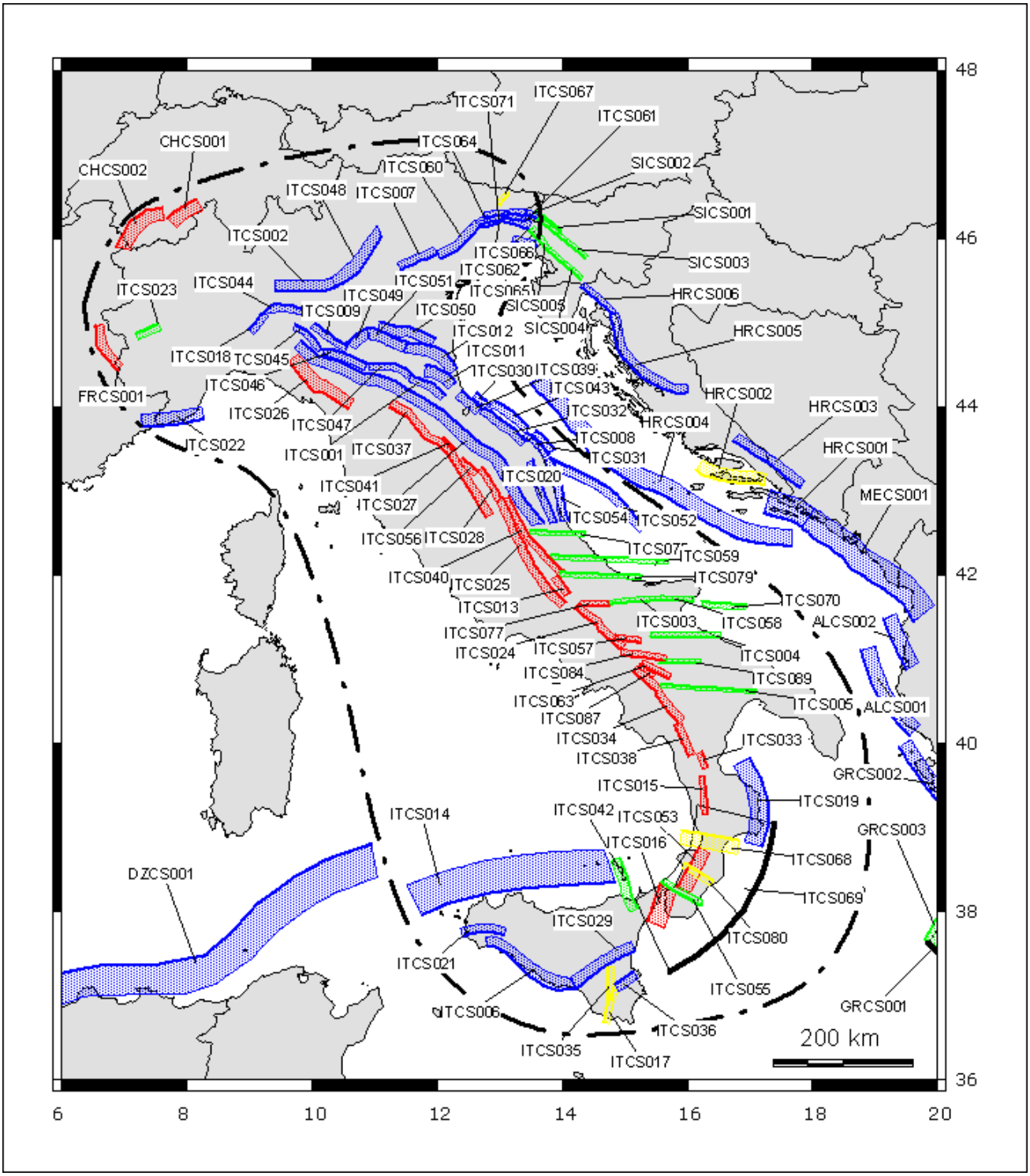

Figure 11. Map of the CSS from the DISS version 3.1.0 database (DISS Working Group, 2009), classified according to faulting mechanism. Red, normal (NN); blue, reverse (RR); green, right-lateral (RL) strike slip; yellow, left-lateral (LL) strike slip; black, subduction. Bold line, top edge of fault; patterned, vertical projection of fault to the ground surface; dashed line, the study area

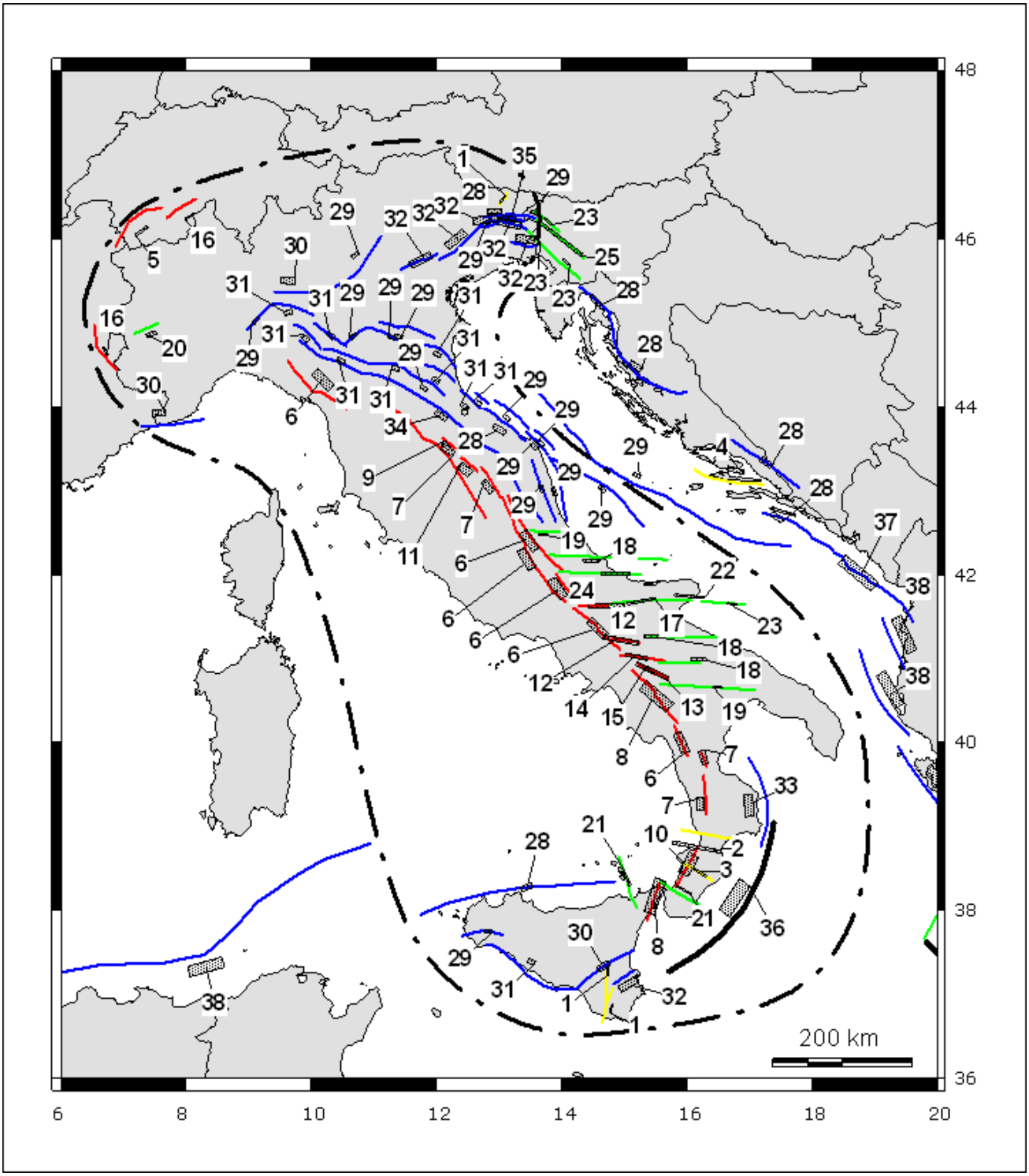

Figure 12. Map of the rectangular grouped typical faults associated with each CSS, and their along-strike floating path. The faulting mechanism is color coded: Red, normal (NN); blue, reverse (RR); green, right-lateral (RL) strike slip; yellow, left-lateral (LL) strike slip

To keep the number of simulations to a minimum, we grouped all of the TFs according to the following "conservative" scheme, based on: magnitude (Table 7), depth of the top of the fault (Table 8), and dip angle (Table 9).

Table 7. The magnitude groups

Group	*TF M*	*Group M*
1	*<= 5.9*	*5.9*
2	*5.9 - 6.3*	*6.3*
3	*6.3 - 6.7*	*6.7*
4	*6.7 - 7.1*	*7.1*

Table 8. The depth-to-top groups

Group	*TF depth (km)*	*Group depth (km)*
1	*<= 4.0*	*1.0*
2	*4.0 – 10.0*	*5.0*
3	*> 10.0*	*10.0*

Table 9. The dip-angle groups

Group	*TF dip (deg)*	*Group dip (deg)*
1	*<= 30*	*25*
2	*30 – 60*	*45*
3	*60 - 90*	*75*

The effects of the grouping are "conservative", as the TFs are clustered according to higher magnitude, and to lower depth and dip angle. Grouping the faults allows us to reduce the number of simulations from over 90 to just 38, with a minimal loss of detail, as can be seen in the list of TFs (Appendix 1)

The maximum observable shaking maps

These MOS maps are designed to represent the seismic potential of the Italian region, as derived from a complete knowledge of the seismogenic sources (the DISS). However, since the concept of MOS maps is a new and innovative approach, the procedure developed here and the corresponding results are still under careful validation.

MOS maps are expressed in terms of the ground-motion parameters of PGA (cm/sec^2), PGV (cm/sec), SI-HI (cm) and SD (cm), and they allow an evaluation of the potential impact of expected earthquakes. Having such a regional overview allows decisions to be made regarding where strong-motion simulations and observations of specific engineering targets need to be investigated in greater detail. This goal can be achieved most efficiently by targeted numerical simulations that cover the parameter range of interest (i.e. in terms of magnitude and distance), and that consider a large suite of earthquake-rupture scenarios.

The simulation parameters

The choices of the simulation parameters take into account the specific needs of the input of the EXSIM program. The approach was carried out as the average, given that we did not aim to retrieve the shaking of a specific single event, but rather a combination of the effects caused by all of the TFs covering the entire national territory.

Furthermore we note that clustering the TFs in a conservative way produces a higher level of shaking. Then, as a first attempt, there was no need for fine differentiation of the crustal properties for each region (e.g. geometric spreading coefficient, Q(f)) or the different properties of the source (e.g. stress drop, nucleation point, rupture velocity).

In the present study, for the evaluation of the HF MOS maps at a national scale, we tested three different models of slip distribution: stochastic (von Karman distribution), random (generated

automatically by EXSIM) and Gaussian. The strike, dip, rake and Mw were taken from the seismogenic sources included in the DISS.

We have generated extended-source rupture models based on a random-field model for complexes, as explained in the previous section for all of the TFs listed in Table 10.

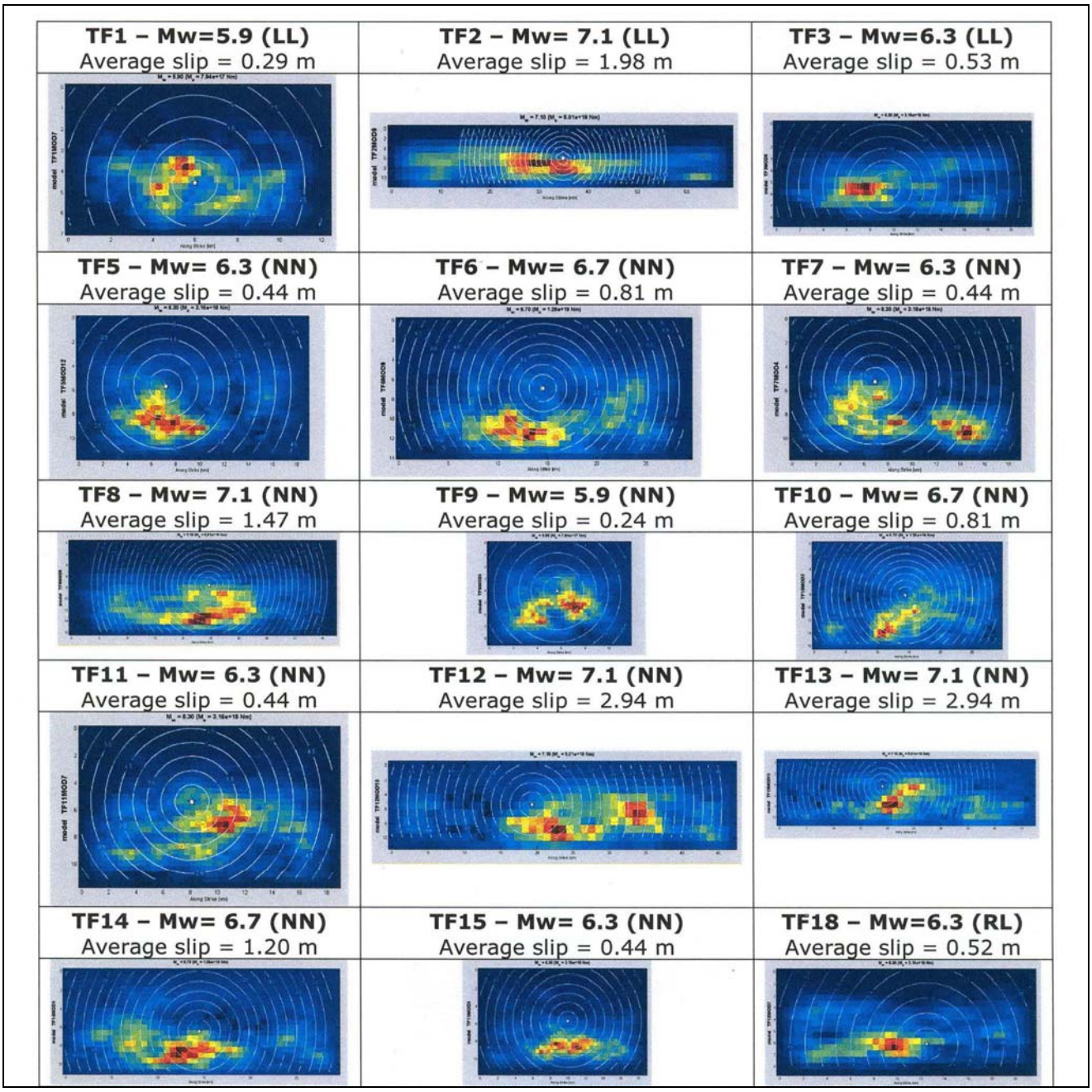

Figure 13: SlipReal stochastic slip maps for the TFG01 to TFG18 of Table 10.

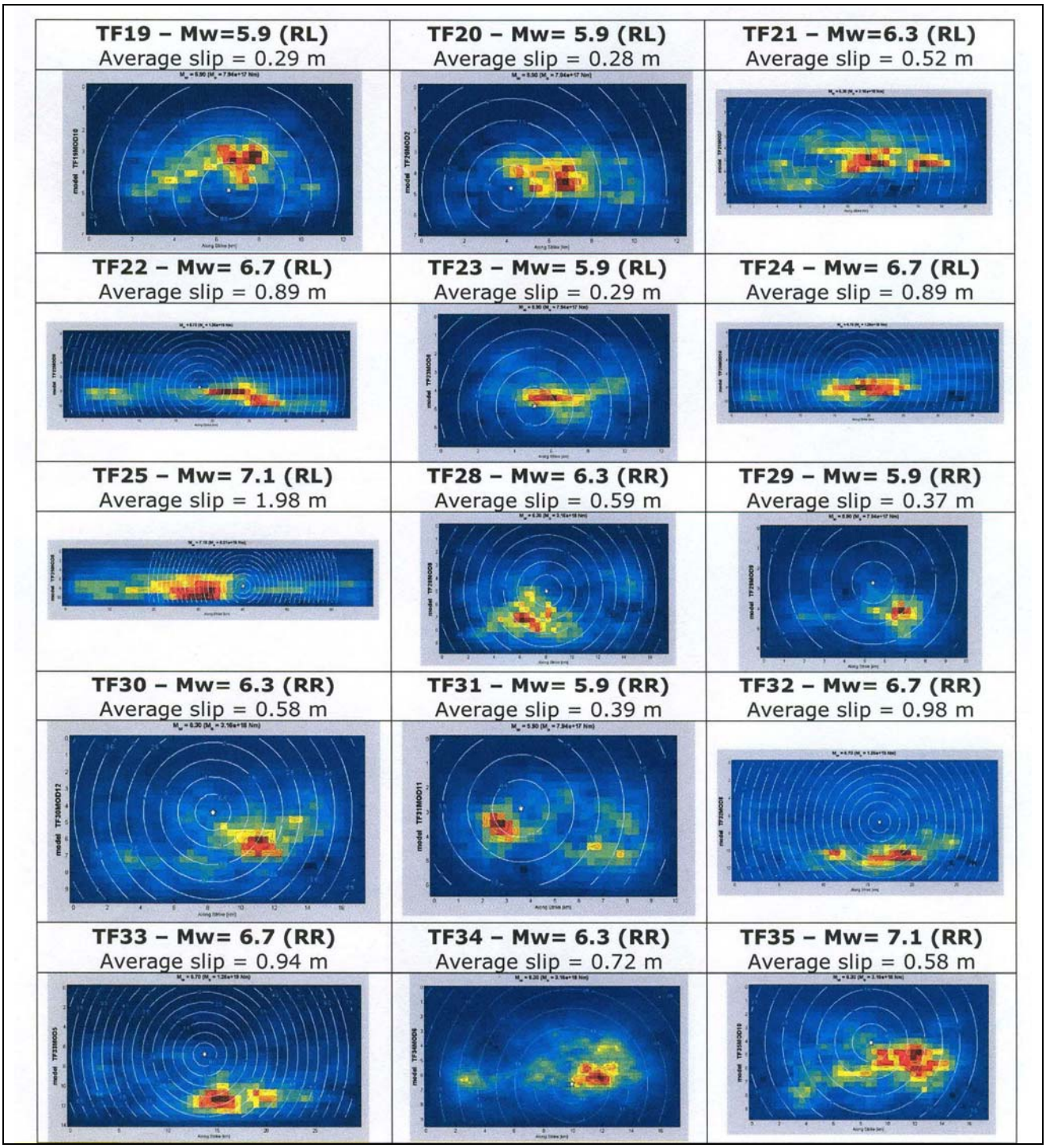

Figure 14 SlipReal stochastic slip maps for TFG19 to TFG35 of Table 10.

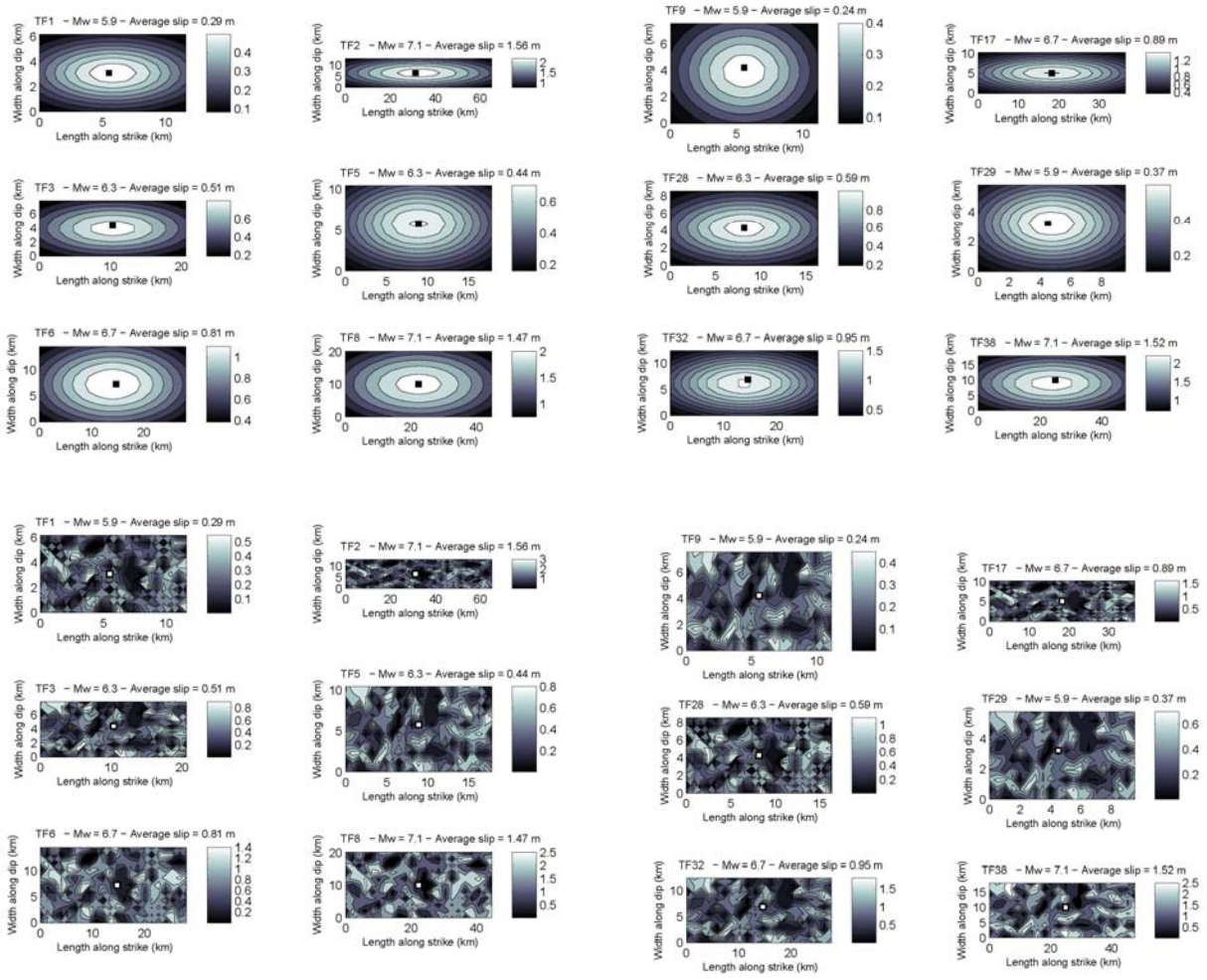

Figure 15. The Gaussian and random slip distributions of the TFs highlighted (gray) in Table 10. In the evaluation of the MOS map, we use bilateral point-of-rupture initiation.

Computation grid around the fault

The contribution of earthquake source complexity to the ground-motion variability is generally believed to be significant, especially in the region of less than one or of two fault lengths distance (Ripperger et. al., 2007). The receiver geometry was organized as a dense regular grid (0.02° × 0.02°) around each fault, and the number of points depended on the length of the fault (see Table 10). The same grid size was adopted for comparisons with the probabilistic map of Italy, covering the entire Italian territory, where each point (longitude and latitude) had an absolute reference label as a research key in the archive.

However, the lateral extent to which the ground shaking was derived was different according to different moment magnitudes, Mw. We considered four major classes: (a) radius of 130 km around the fault, for a total of 10,439 points (TFG02, TFG25 and TFG38); (b) radius of 100 km, for a total of 6,242 points (TFG08, TFG12, TFG13 and TFG36); (c) radius of 80 km, for a total of 3,943 points (TFG17, TFG22 and TFG24); and (d) radius of 60 km, for a total of 2,132 points for all of the other TFs. To reduce the computing time, the number of stochastic realizations was limited to 30, which meant an average of 45 s for each point, with a fixed number of sub-faults and a sampling of 0.01 (s).

In the future, we will generate less dense, but adequately sampled, receiver grids around the faults, considering NF/FF simulations; this grid will be denser close to the fault, and then less dense farther away from the fault.

During the stochastic simulations described above, the acceleration and velocity time histories matching the mean values were stored for each grid point of the fault. The upper left point and the projection of the other corners of the fault on the surface were considered as appropriate "anchor" points with respect to the grid, for the later geographic information systems (GIS) floating and interpolation of the shaking parameters.

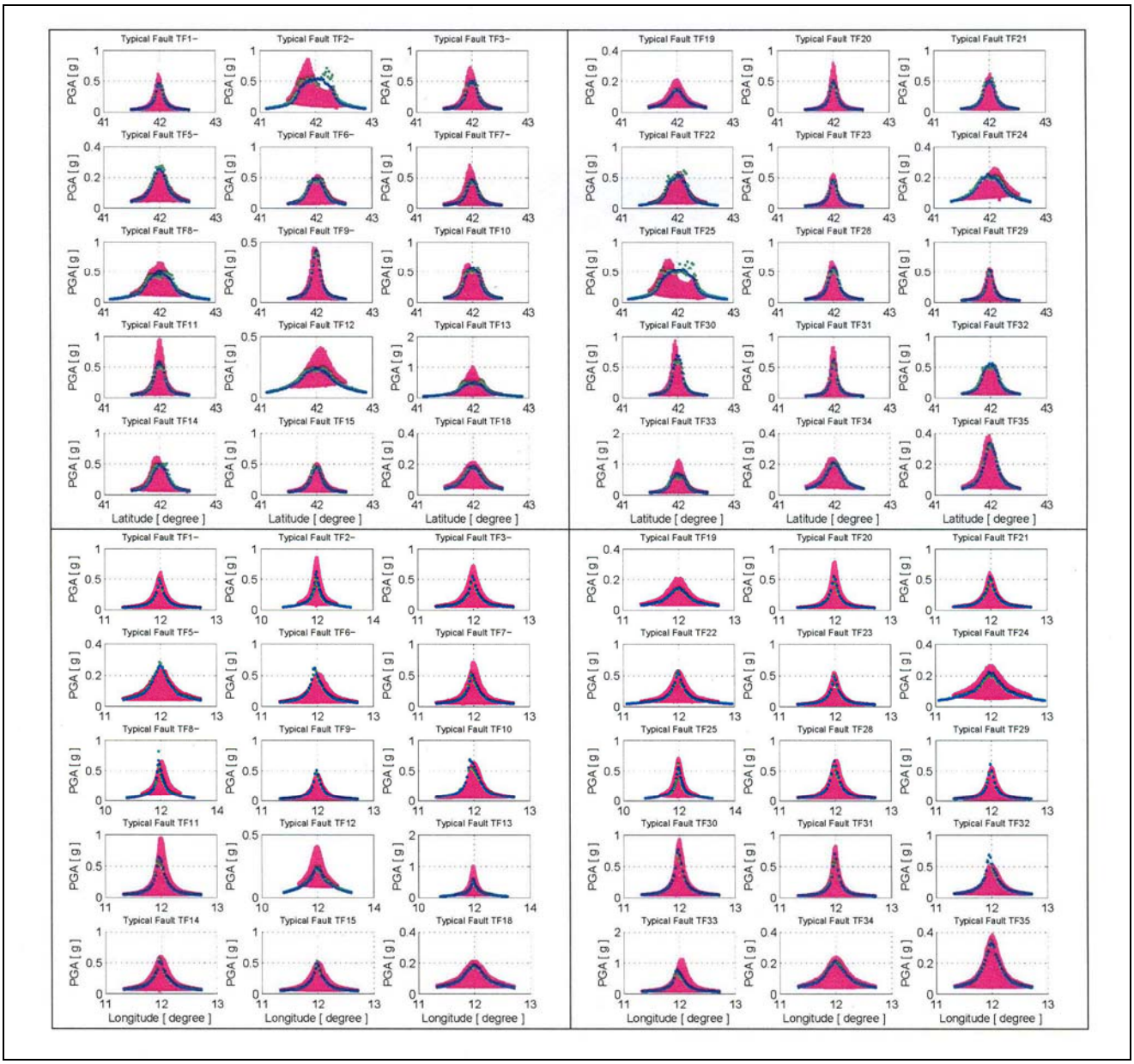

Figure 16. Comparisons of the simulated ground-motion PGA(g) values obtained on grid points around the different TFs using different slip distributions: SlipReal (pink), random (green) and Gaussian (blue)

GIS floating on the segmentation

From the conceptual point of view, the CSS includes an active tectonic structure at a regional scale. The geometric and kinematic properties of the structure are assumed to show only limited variations inside the CSS; similarly, the rheological and dynamic properties of the tectonic structure are assumed to allow equally large earthquakes to be released throughout all of the CSS.

Table 10. The grouped TFs according to the moment magnitudes and faulting mechanisms. The typical slip distributions (Gaussian and random) have been considered for the shaded-code

ID group	Fault type	Length	Width	Slip	Mw	Moment	Dip	Rake	Depth to top	Depth to bottom	ID source
		(km)	(km)	(m)		(Nm)	(°)	(°)	(km)	(km)	
TFG01	LL	12.2	6.8	0.356	5.9	8.91E+17	75	0	1.0	7.6	ITCS017/ITCS035/ITCS067/
TFG02	LL	67.9	14.4	1.923	7.1	5.62E+19	75	350	1.0	14.9	ITCS068/
TFG03	LL	21.7	8.7	0.625	6.3	3.55E+18	75	315	1.0	9.4	ITCS080/
TFG05	NN	18.6	11.6	0.547	6.3	3.55E+18	75	270	5.0	16.2	CHCS002/
TFG06	NN	29.5	16.0	0.995	6.7	1.41E+19	45	270	1.0	12.3	ITCS013/ITCS024/ITCS025/ITCS026/ITCS038/ITCS040/
TFG07	NN	18.6	11.6	0.547	6.3	3.55E+18	45	270	1.0	9.2	ITCS015/ITCS028/ITCS033/ITCS037/
TFG08	NN	46.8	22.1	1.811	7.1	5.62E+19	45	265	1.0	16.6	ITCS016/ITCS034/
TFG09	NN	11.7	8.4	0.301	5.9	8.91E+17	45	270	1.0	6.9	ITCS041/
TFG10	NN	29.5	16.0	0.995	6.7	1.41E+19	25	270	1.0	7.8	ITCS053/
TFG11	NN	18.6	11.6	0.547	6.3	3.55E+18	25	270	1.0	5.9	ITCS056/
TFG12	NN	46.8	22.1	1.811	7.1	5.62E+19	75	230	10.0	31.4	ITCS057/ITCS077/
TFG13	NN	46.8	22.1	1.811	7.1	5.62E+19	75	240	1.0	22.4	ITCS063/
TFG14	NN	29.5	16.0	0.995	6.7	1.41E+19	75	240	1.0	16.5	ITCS084/
TFG15	NN	18.6	11.6	0.547	6.3	3.55E+18	75	270	1.0	12.2	ITCS087/
TFG16	NN	11.7	8.4	0.301	5.9	8.91E+17	75	270	5.0	13.1	CHCS001/FRCS001/
TFG17	RL	38.4	11.2	1.096	6.7	1.41E+19	75	200	5.0	15.8	ITCS003/
TFG18	RL	21.7	8.7	0.625	6.3	3.55E+18	75	180	10.0	18.4	ITCS004/ITCS059/ITCS089/
TFG19	RL	12.2	6.8	0.356	5.9	8.91E+17	75	180	10.0	16.6	ITCS005/ITCS075/
TFG20	RL	12.2	6.8	0.356	5.9	8.91E+17	45	143	1.0	5.8	ITCS023/
TFG21	RL	21.7	8.7	0.625	6.3	3.55E+18	75	200	1.0	9.4	ITCS042/ITCS055/
TFG22	RL	38.4	11.2	1.096	6.7	1.41E+19	75	215	1.0	11.8	ITCS058/
TFG23	RL	12.2	6.8	0.356	5.9	8.91E+17	75	175	1.0	7.6	ITCS070/SICS001/SICS004/SICS005/
TFG24	RL	38.4	11.2	1.096	6.7	1.41E+19	75	200	10.0	20.8	ITCS079/
TFG28	RR	17.1	9.4	0.734	6.3	3.55E+18	45	90	1.0	7.6	HRCS001/HRCS003/HRCS005/HRCS006/ITCS014/ITCS032/ITCS064/
TFG29	RR	10.0	6.4	0.459	5.9	8.91E+17	45	85	1.0	5.6	HRCS004/ITCS001/ITCS008/ITCS018/ITCS020/ITCS021/ITCS031/ITCS043/ITCS048/ITCS049/ITCS050/ITCS051/ITCS052/ITCS054/ITCS071/SICS003/
TFG30	RR	17.1	9.4	0.734	6.3	3.55E+18	25	90	1.0	5.0	ITCS002/ITCS022/ITCS029/
TFG31	RR	10.0	6.4	0.459	5.9	8.91E+17	25	100	1.0	3.7	ITCS006/ITCS009/ITCS011/ITCS012/ITCS030/ITCS039/ITCS044/ITCS045/ITCS046/ITCS047/
TFG32	RR	29.2	13.7	1.175	6.7	1.41E+19	45	90	1.0	10.7	ITCS007/ITCS036/ITCS060/ITCS062/ITCS065/ITCS066/
TFG33	RR	29.2	13.7	1.175	6.7	1.41E+19	25	90	1.0	6.8	ITCS019/
TFG34	RR	17.1	9.4	0.734	6.3	3.55E+18	45	90	10.0	16.6	ITCS027/
TFG35	RR	17.1	9.4	0.734	6.3	3.55E+18	45	100	5.0	11.6	ITCS061/
TFG36	RR	49.9	20.0	1.879	7.1	5.62E+19	25	90	10.0	18.5	ITCS069/
TFG38	RR	49.9	20.0	1.879	7.1	5.62E+19	45	90	1.0	15.1	ALCS001/ALCS002/DZCS001/GRCS002/

This procedure allows a number of potential scenarios to be explored, based on the information that is more robust (the location and geometry of the fault(s)), without having to consider the exact location of the ends of the co-seismic rupture. In other words, the limited knowledge of the internal structure of the CSS, and hence of any permanent segment boundaries, was allowed for by simply ignoring the possibility that these boundaries exist.

From the operational point of view, the CSS had to be spatially segmented at regular intervals, and to overlap with the fault floating along the width of the CSS. The regular intervals of the spatial segmentation had to be a balance between the best smoothing and the time that the GIS floating and interpolation of the shaking parameters needed. The total number of segmentations was 8,859 patches for the whole of Italy. The float computation of the MOS map by the GIS was carried out using an affine transformation procedure; with a similarity rotation and translation performed (all of the coordinates were updated through a least-square error solution applied to the geographic control points of the GIS coverage). The transformed coverage for each TF was overlaid, and a grid with the maximum values for the MOS map was evaluated for the CSS. On the MOS map, we then plotted the maximum values of the simulated shaking parameters at each point of the grid, as caused by a scenario earthquake in each TF included over the whole Italian country.

Results of the MOS evaluation

To evaluate the MOS maps, we considered the distribution of CCS (Fig. 11) and the grouped TFs (Fig. 12) listed in Table 10. We also considered TFG38 (Mw 7.1), because even outside the national territory, we felt that its contribute would not be negligible in terms of the shaking on the coast of the Puglia region. We used all of the input parameters of the EXSIM program (Table 1).

The maps were computed using the Gaussian slip distributions with the nucleation point in the middle of the fault. Even if there were 33 TFs (see Table 10), we had to calculate only 12 different slip distributions because there are some of the same size: TFG01 also represents TFG19, TFG20 and TFG23; TFG02 also represents TFG25; TFG03 also represents TFG18 and TFG21; TFG05 also represents TFG07, TFG11 and TFG15; TFG06 also represents TFG10 and TFG14; TFG08 also represents TFG12 and TFG13; TFG09 also represents TFG16; TFG17 also represents TFG22 and TFG24; TFG28 also represents TFG30, TFG34 and TFG35; TFG29 also represents TFG31; TFG32 also represents TFG33 (see Table 10). The MOS results in terms of PGA (g) and PGV (cm/sec) are shown in Figure 17.

HF MOS map in terms of PGA (Gaussian)	HF MOS map in terms of PGV(Gaussian)

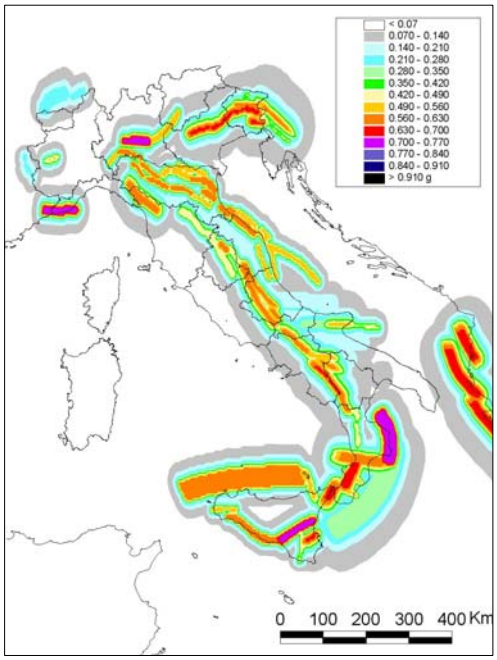

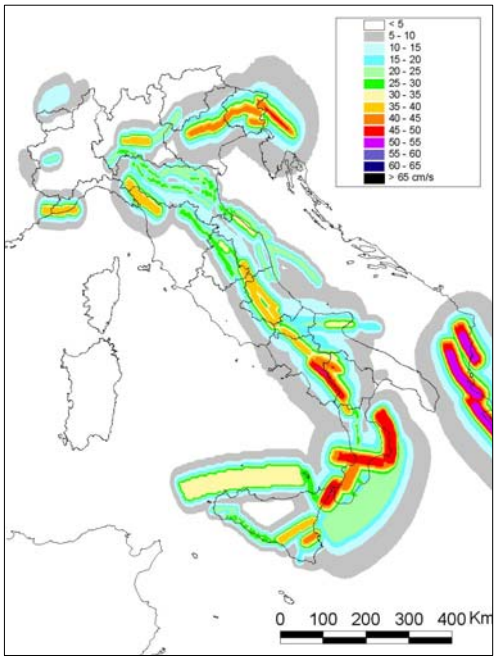

HF MOS map in terms of SI (Gaussian)	HF MOS map in terms of SD_{10sec}(Gaussian)

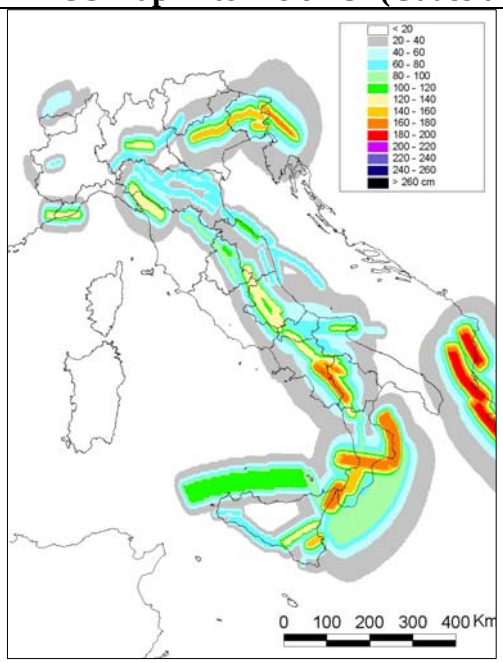

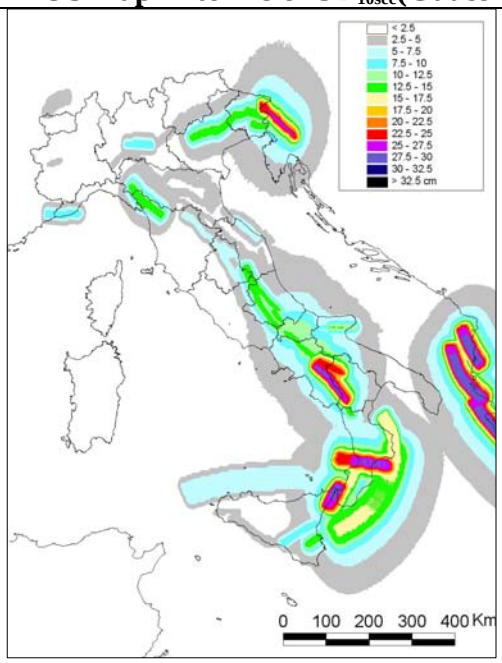

Figure 17. HF MOS maps in terms of PGA (g), PGV (cm/sec), SI-HI (cm) and SD_{10sec} (cm) using the Gaussian slip distribution.

The HF MOS maps in terms of PGA(g), PGV(cm/sec), SI-HI (cm) and SD_{10sec} (cm) covered the whole of Italy and show an overview of the seismic hazard for large areas using the fault sources directly. The shaking maps obtained are referred to the bedrock level, without considering site effects. The results arise from some assumptions, like no regionalization, and we have used the same simulation parameters for all of the regions, and assumed *a-priori* conservative grouping criteria (see Tables 7, 8 and 9).

Figure 18 shows the HF MOS map in terms of PGA(g), PGV(cm/sec), SI-HI (cm) and SD_{10sec} (cm) using the random slip distribution with bilateral point-of-rupture initiation.

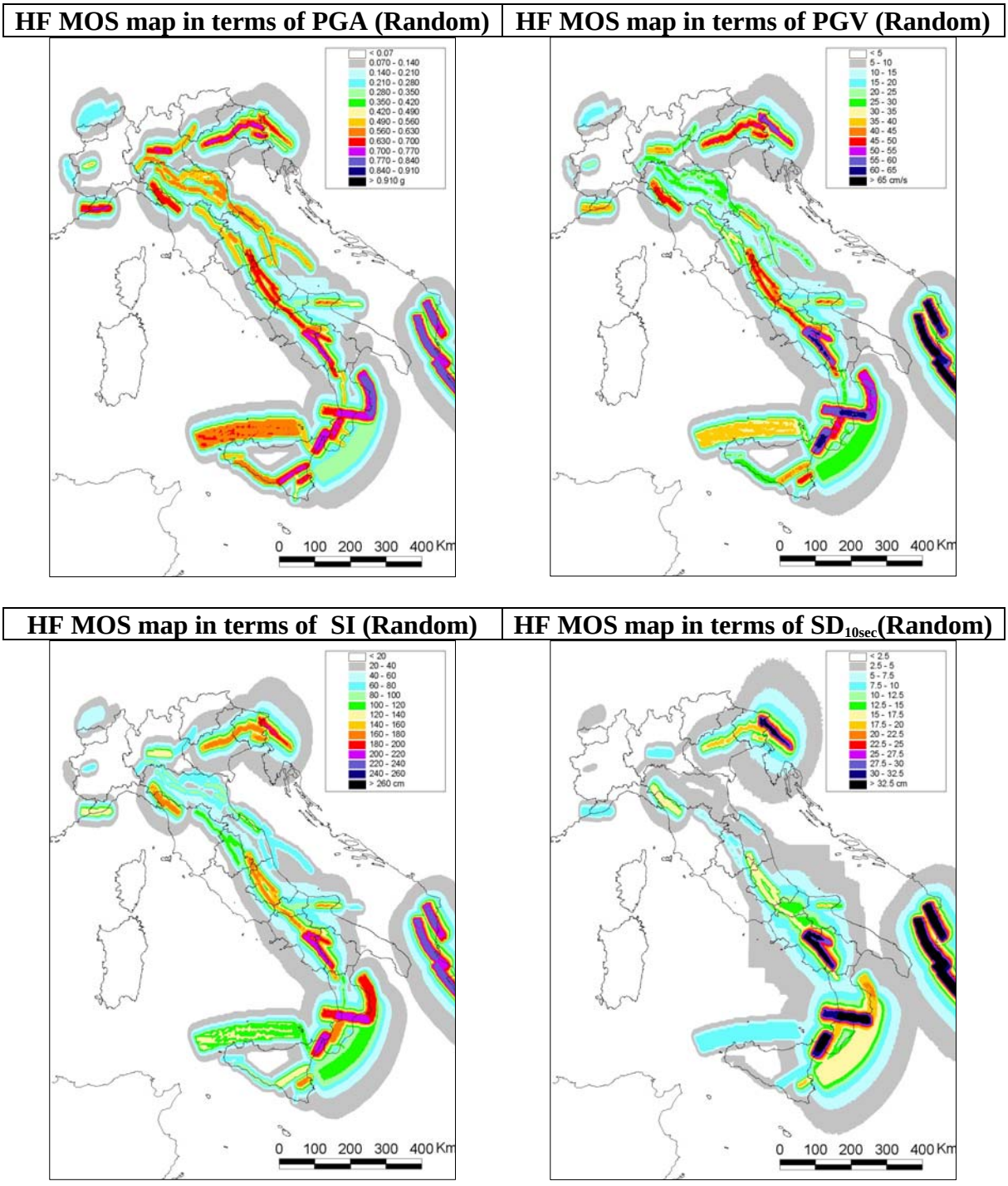

Figure 18. HF MOS maps in terms of PGA (g), PGV (cm/sec), SI-HI (cm) and SD_{10sec} (cm) using the random slip distribution.

Conclusions

This study presents the innovative concept of maximum observable shaking (MOS) maps that makes use of the improved understanding of the Italian regional tectonic setting and uses composite seismic sources (CSS) taken from an Italian database of individual seismic sources.

The MOS maps are expressed in terms of the ground-motion parameters of PGA (cm/sec^2), PGV (cm/sec), SI-HI (cm) and SD (cm), and they allow an evaluation of the potential impact of expected earthquakes. Having such a regional overview allows decisions to be made regarding where strong-motion simulations and observations of specific engineering targets need to be investigated in greater detail.

This goal can be achieved most efficiently by targeted numerical simulations that cover the parameter range of interest (i.e. in terms of magnitude and distance), and that consider a large suite of earthquake-rupture scenarios.

2 Relevance for DPC and/or for the scientific community

MOS maps are meant to represent the seismic potential for the Italian region as they are derived from the complete knowledge of the seismogenic sources (the DISS). They offer an overall view on the entire Italy on where a given range of shaking might occur in response of a future earthquake. However, since the concept of MOS maps is a new and innovative approach, the procedure developed here has been applied only to High-Frequency range.

3 Changes with respect to the original plans and reasons for it

We had fruitfully reached the goal to deliver the computation of Maximum Observable Shaking (MOS) maps of Italy using a finite-fault stochastic approach.

However we made important changes:

- a general framework to evaluate the MOS map has been formalize only for the HF frequency range but not yet for the complete wavefield broadband simulations
- the single individual source was used for single site analysis or to study specific past earthquake while the Typical Faults have been used in computing the HF MOS map for the entire Italian Territory floating the faults along the Composite Seismic Sources;
- the HF MOS maps are expressed in terms of not only two ground-motion parameters PGA (cm/sec^2) and SI-Housner (cm) but also in PGV (cm/sec) and SD (cm).

References

Barba, S. and Basili, R. (2000). Analysis of seismological and geological observations for moderate size earthquakes: the Colfiorito Fault System (Central Apennines, Italy). Geophys. J. Int.,141, 241-252, doi:10.1046/j.1365-246X.2000.00080.x.

Basili, R., Valensise, G., Vannoli, P., Burrato, P., Fracassi, U., Mariano, S., Tiberti, M.M. and Boschi, E., (2008). The Database of Individual Seismogenic Sources (DISS), version 3: summarizing 20 years of research on Italy's earthquake geology, Tectonophysics, 453, 20-43, doi:10.1016/j.tecto.2007.04.014.

Beresnev, I. A. and Atkinson, G. M. (1998). FINSIM - a FORTRAN program for simulating stochastic acceleration time histories from finite faults, Seismological Research Letters 69, 27-32.

Boore, D.M. (2003). Simulation of ground motion using the stochastic method. Pure Appl Geophys 160:635–676

Boore, D. M. (2009). Comparing stochastic point- and finite-source ground-motion simulations: SMSIM and EXSIM, Bull. Seism. Soc. Am., Vol. 99, No. 6, pp. 3202–3216, December 2009, doi: 10.1785/0120090056

DISS Working Group (2009). Database of Individual Seismogenic Sources (DISS), Version 3.1.0: A compilation of potential sources for earthquakes larger than M 5.5 in Italy and surrounding areas. http://diss.rm.ingv.it/diss/, © INGV 2009 - Istituto Nazionale di Geofisica e Vulcanologia

Gail, M., Atkinson, G., M., Assatourians, K., Boore, D., M., Campbell, K., and Motazedian D. (2009). A Guide to Differences between Stochastic Point-Source and Stochastic Finite-Fault Simulations, Bulletin of the Seismological Society of America, Vol. 99, No. 6, pp. 3192–3201.

Imperatori, W., and Mai, P.M. (2009). Broadband Ground Motion Simulations in the Messina Strait Area (Southern Italy): Appraising Strong Motion Variability due to Complexity in Source and Earth Structure, manuscript in preparation

Kanamori, H., and Brodsky, E.E. (2004). The physics of earthquakes, Rep. Prog. Phys., 67(8), 1429– 1496.

Lorito, S., Tiberti, M.M., Basili, R., Piatanesi, A., and Valensise, G. (2008). Earthquake-generated tsunamis in the Mediterranean Sea: Scenarios of potential threats to Southern Italy. Jour. Geophy. Res., 113, b01301, doi:10.1029/2007jb004943.

Mai, P.M., and Beroza G., (2000). Source-scaling properties from finite-fault rupture models, Bull. Seis. Soc. Am., 90 (3), 604-615.

Mai, P.M., and Beroza, G. (2002). A spatial random-field model to characterize complexity in earthquake slip, J. Geophys. Res., 107(B11), 2308, doi:10.1029/2001JB000588, 2002.

Mai, P.M, and Beroza G. (2003). A hybrid method for calculating near-source, broadband seismograms: application to strong motion prediction. Physics of the Earth and Planet. Int., 137: 183-199

Mai, P.M., and Olsen K.B. (2005). Broadband ground-motion simulations using finite-difference synthetics and local scattering operators, Annual Report to the Southern California Earthquake Center (SCEC), November 2005.

Mai, P.M., Spudich, P. and Boatwright J. (2005). Hypocenter locations in finite-source rupture models. Bull. Seis. Soc. Am, 95(3): 965-980.

Mena, B., Mai, P.M., Olsen, K.B., Purvance, M.D. and Brune J.N. (2009). Hybrid broadband ground motions simulation using scattering Greens functions: application to large magnitude events, revised for Bull. Seis. Soc. Am.

Motazedian, D., and Atkinson G.M. (2005). Stochastic Finite-Fault Modeling Based on a Dynamic Corner Frequency. Bull. Seis. Soc. Am, 95(3): 995–1010.

Ponziani, F., De Franco, R., Minelli, G., Biella, G., Federico, C. and Pialli G. (1990). Crustal shortening and duplication of the Moho in the Northern Apennines: a view from seismic refraction data, Tectonophysics, 252, 391–418.

Ripperger,. J, Mai, P.M. and Ampuero J.P. (2008). Variability of Near-Field Ground Motion from Dynamic Earthquake Rupture Simulations. accepted for Bull. Seis. Soc. Am.

Spudich, P., and Archuleta, R. (1987). Techniques for earthquake ground motion calculation with applications to source parametrization of finite faults, in Bolt, B. A. ad., SEISMIC STRONG MOTION SYNTHETICS: Orlando, Florida, Academic Press, p. 205-265.

Spudich, P., and Xu, L. (2003). Documentation of software package COMPSYN and ISOSYN sxv3.11. In: International Handbook of Earthquake and Engineering Seismology CD, IASPEI, Academic Press, 74 pp.

Stucchi et al. (2007). DBMI04, il database delle osservazioni macrosismiche dei terremoti italiani utilizzate per la compilazione del catalogo parametrico CPTI04. Quaderni di Geofisica, Vol 49, pp.38. http://emidius.mi.ingv.it/DBMI04/

Valensise, G., and Pantosti, D. (eds.), (2001). Database of potential sources for earthquakes larger than M 5.5 in Italy. Ann. Geofis., Suppl. to vol. 44(4), 797–964, with CD-ROM.

Wells, D.L., and Coppersmith K.J. (1994). New empirical relationships among magnitude, rupture length, rupture width, rupture area, and surface displacement. Bull. Sesmic Soc. Am. 84, 974-1002.

Zonno, G., Musacchio, G., Basili, R., Imperatori, W., and Mai P.M. (2008). Stochastic and full-wavefield finite-fault round-motion simulations of the M 7.1, Messina 1908 Earthquake (Southern Italy). Abstract presented at the A.G.U. Fall Meeting 2008, San Francisco (CA-USA), December 2008. http://hdl.handle.net/2122/4742

APPENDIX 1 All of the TFs (ungrouped and grouped)

Typical faults							Typical faults after grouping							
ID-CSS	Type	Length (km)	Width (km)	Dip (°)	Depth (km)	Mw	IDGroup	Length (km)	Width (km)	Dip (°)	Depth (km)	Slip (m)	Moment (Nm)	Mw
CHCS001	NN	11.7	8.4	65	5.0	5.9	TFG16	11.7	8.4	75	5.0	0.30	8.9E+17	5.9
CHCS002	NN	14.8	9.9	65	5.0	6.1	TFG5	18.6	11.6	75	5.0	0.55	3.5E+18	6.3
FRCS001	NN	6.6	5.6	65	5.0	5.4	TFG16	11.7	8.4	75	5.0	0.30	8.9E+17	5.9
ITCS001	RR	8.8	5.9	35	2.0	5.8	TFG29	10.0	6.4	45	1.0	0.46	8.9E+17	5.9
ITCS002	RR	15.0	8.6	30	1.0	6.2	TFG30	17.1	9.4	25	1.0	0.73	3.5E+18	6.3
ITCS003	RL	38.4	11.2	85	6.0	6.7	TFG17	38.4	11.2	75	5.0	1.10	1.4E+19	6.7
ITCS004	RL	21.7	8.7	80	11.0	6.3	TFG18	21.7	8.7	75	10.0	0.62	3.5E+18	6.3
ITCS005	RL	10.6	6.4	85	13.0	5.8	TFG19	12.2	6.8	75	10.0	0.36	8.9E+17	5.9
ITCS006	RR	5.9	4.4	30	3.0	5.5	TFG31	10.0	6.4	25	1.0	0.46	8.9E+17	5.9
ITCS007	RR	25.6	12.5	35	0.5	6.6	TFG32	29.2	13.7	45	1.0	1.17	1.4E+19	6.7
ITCS008	RR	8.8	5.9	37	3.0	5.8	TFG29	10.0	6.4	45	1.0	0.46	8.9E+17	5.9
ITCS009	RR	6.7	4.9	30	2.0	5.6	TFG31	10.0	6.4	25	1.0	0.46	8.9E+17	5.9
ITCS011	RR	10.0	6.4	30	3.0	5.9	TFG31	10.0	6.4	25	1.0	0.46	8.9E+17	5.9
ITCS012	RR	6.7	4.9	30	2.0	5.6	TFG31	10.0	6.4	25	1.0	0.46	8.9E+17	5.9
ITCS013	NN	20.9	12.6	60	1.0	6.4	TFG6	29.5	16.0	45	1.0	1.00	1.4E+19	6.7
ITCS014	RR	15.0	8.6	42	2.0	6.2	TFG28	17.1	9.4	45	1.0	0.73	3.5E+18	6.3
ITCS015	NN	16.6	10.7	60	1.0	6.2	TFG7	18.6	11.6	45	1.0	0.55	3.5E+18	6.3
ITCS016	NN	41.7	20.4	32	2.0	7.0	TFG8	46.8	22.1	45	1.0	1.81	5.6E+19	7.1
ITCS017	LL	6.9	5.3	80	1.0	5.5	TFG1	12.2	6.8	75	1.0	0.36	8.9E+17	5.9
ITCS018	RR	5.9	4.4	32	2.0	5.5	TFG29	10.0	6.4	45	1.0	0.46	8.9E+17	5.9
ITCS019	RR	22.4	11.4	30	3.0	6.5	TFG33	29.2	13.7	25	1.0	1.17	1.4E+19	6.7
ITCS020	RR	10.0	6.4	40	3.0	5.9	TFG29	10.0	6.4	45	1.0	0.46	8.9E+17	5.9
ITCS021	RR	6.7	4.9	50	3.0	5.6	TFG29	10.0	6.4	45	1.0	0.46	8.9E+17	5.9
ITCS022	RR	17.1	9.4	30	3.0	6.3	TFG30	17.1	9.4	25	1.0	0.73	3.5E+18	6.3
ITCS023	RL	9.2	6.0	45	1.0	5.7	TFG20	12.2	6.8	45	1.0	0.36	8.9E+17	5.9
ITCS024	NN	26.3	14.8	55	1.0	6.6	TFG6	29.5	16.0	45	1.0	1.00	1.4E+19	6.7
ITCS025	NN	29.5	16.0	57	1.0	6.7	TFG6	29.5	16.0	45	1.0	1.00	1.4E+19	6.7
ITCS026	NN	23.4	13.6	37	1.0	6.5	TFG6	29.5	16.0	45	1.0	1.00	1.4E+19	6.7
ITCS027	RR	15.0	8.6	37	12.0	6.2	TFG34	17.1	9.4	45	10.0	0.73	3.5E+18	6.3
ITCS028	NN	18.6	11.6	40	2.5	6.3	TFG7	18.6	11.6	45	1.0	0.55	3.5E+18	6.3
ITCS029	RR	11.5	7.1	30	3.0	6.0	TFG30	17.1	9.4	25	1.0	0.73	3.5E+18	6.3

ITCS030	RR	10.0	6.4	30	3.0	5.9	TFG31	10.0	6.4	25	1.0	0.46	8.9E+17	5.9
ITCS031	RR	10.0	6.4	37	2.0	5.9	TFG29	10.0	6.4	45	1.0	0.46	8.9E+17	5.9
ITCS032	RR	13.1	7.8	32	2.5	6.1	TFG28	17.1	9.4	45	1.0	0.73	3.5E+18	6.3
ITCS033	NN	16.6	10.7	60	1.0	6.2	TFG7	18.6	11.6	45	1.0	0.55	3.5E+18	6.3
ITCS034	NN	33.1	17.4	60	1.0	6.8	TFG8	46.8	22.1	45	1.0	1.81	5.6E+19	7.1
ITCS035	LL	8.0	5.6	75	1.0	5.6	TFG1	12.2	6.8	75	1.0	0.36	8.9E+17	5.9
ITCS036	RR	25.6	12.5	45	3.0	6.6	TFG32	29.2	13.7	45	1.0	1.17	1.4E+19	6.7
ITCS037	NN	16.6	10.7	32	0.5	6.2	TFG7	18.6	11.6	45	1.0	0.55	3.5E+18	6.3
ITCS038	NN	20.9	12.6	60	1.0	6.4	TFG6	29.5	16.0	45	1.0	1.00	1.4E+19	6.7
ITCS039	RR	7.7	5.3	30	3.0	5.7	TFG31	10.0	6.4	25	1.0	0.46	8.9E+17	5.9
ITCS040	NN	23.4	13.6	60	1.0	6.5	TFG6	29.5	16.0	45	1.0	1.00	1.4E+19	6.7
ITCS041	NN	10.5	7.8	45	1.0	5.8	TFG9	11.7	8.4	45	1.0	0.30	8.9E+17	5.9
ITCS042	RL	16.3	7.7	80	1.0	6.1	TFG21	21.7	8.7	75	1.0	0.62	3.5E+18	6.3
ITCS043	RR	5.9	4.4	37	2.5	5.5	TFG29	10.0	6.4	45	1.0	0.46	8.9E+17	5.9
ITCS044	RR	5.9	4.4	30	2.0	5.5	TFG31	10.0	6.4	25	1.0	0.46	8.9E+17	5.9
ITCS045	RR	5.9	4.4	30	2.0	5.5	TFG31	10.0	6.4	25	1.0	0.46	8.9E+17	5.9
ITCS046	RR	10.0	6.4	30	2.0	5.9	TFG31	10.0	6.4	25	1.0	0.46	8.9E+17	5.9
ITCS047	RR	6.7	4.9	30	2.0	5.6	TFG31	10.0	6.4	25	1.0	0.46	8.9E+17	5.9
ITCS048	RR	7.7	5.3	35	1.0	5.7	TFG29	10.0	6.4	45	1.0	0.46	8.9E+17	5.9
ITCS049	RR	5.9	4.4	40	3.0	5.5	TFG29	10.0	6.4	45	1.0	0.46	8.9E+17	5.9
ITCS050	RR	5.9	4.4	40	1.0	5.5	TFG29	10.0	6.4	45	1.0	0.46	8.9E+17	5.9
ITCS051	RR	10.0	6.4	35	3.0	5.9	TFG29	10.0	6.4	45	1.0	0.46	8.9E+17	5.9
ITCS052	RR	5.9	4.4	37	3.0	5.5	TFG29	10.0	6.4	45	1.0	0.46	8.9E+17	5.9
ITCS053	NN	26.3	14.8	30	3.0	6.6	TFG10	29.5	16.0	25	1.0	1.00	1.4E+19	6.7
ITCS054	RR	5.9	4.4	40	3.0	5.5	TFG29	10.0	6.4	45	1.0	0.46	8.9E+17	5.9
ITCS055	RL	14.1	7.2	70	3.0	6.0	TFG21	21.7	8.7	75	1.0	0.62	3.5E+18	6.3
ITCS056	NN	13.2	9.1	20	2.0	6.0	TFG11	18.6	11.6	25	1.0	0.55	3.5E+18	6.3
ITCS057	NN	37.2	18.8	70	11.0	6.9	TFG12	46.8	22.1	75	10.0	1.81	5.6E+19	7.1
ITCS058	RL	25.0	9.3	85	0.0	6.4	TFG22	38.4	11.2	75	1.0	1.10	1.4E+19	6.7
ITCS059	RL	14.1	7.2	80	11.0	6.0	TFG18	21.7	8.7	75	10.0	0.62	3.5E+18	6.3
ITCS060	RR	22.4	11.4	40	1.0	6.5	TFG32	29.2	13.7	45	1.0	1.17	1.4E+19	6.7
ITCS061	RR	13.1	7.8	35	6.0	6.1	TFG35	17.1	9.4	45	5.0	0.73	3.5E+18	6.3
ITCS062	RR	22.4	11.4	35	1.0	6.5	TFG32	29.2	13.7	45	1.0	1.17	1.4E+19	6.7
ITCS063	NN	37.2	18.8	70	2.0	6.9	TFG13	46.8	22.1	75	1.0	1.81	5.6E+19	7.1
ITCS064	RR	15.0	8.6	37	1.0	6.2	TFG28	17.1	9.4	45	1.0	0.73	3.5E+18	6.3

ITCS065	RR	19.6	10.3	45	0.5	6.4	TFG32	29.2	13.7	45	1.0	1.17	1.4E+19	6.7
ITCS066	RR	22.4	11.4	35	2.0	6.5	TFG32	29.2	13.7	45	1.0	1.17	1.4E+19	6.7
ITCS067	LL	10.6	6.4	75	1.0	5.8	TFG1	12.2	6.8	75	1.0	0.36	8.9E+17	5.9
ITCS068	LL	51.1	12.7	80	3.0	6.9	TFG2	67.9	14.4	75	1.0	1.92	5.6E+19	7.1
ITCS069	RR	49.9	20.0	30	11.0	7.1	TFG36	49.9	20.0	25	10.0	1.88	5.6E+19	7.1
ITCS070	RL	6.9	5.3	85	1.0	5.5	TFG23	12.2	6.8	75	1.0	0.36	8.9E+17	5.9
ITCS071	RR	10.0	6.4	35	0.5	5.9	TFG29	10.0	6.4	45	1.0	0.46	8.9E+17	5.9
ITCS075	RL	9.2	6.0	80	11.0	5.7	TFG19	12.2	6.8	75	10.0	0.36	8.9E+17	5.9
ITCS077	NN	41.7	20.4	70	11.0	7.0	TFG12	46.8	22.1	75	10.0	1.81	5.6E+19	7.1
ITCS079	RL	33.3	10.5	80	11.0	6.6	TFG24	38.4	11.2	75	10.0	1.10	1.4E+19	6.7
ITCS080	LL	14.1	7.2	70	3.0	6.0	TFG3	21.7	8.7	75	1.0	0.62	3.5E+18	6.3
ITCS084	NN	29.5	16.0	65	1.0	6.7	TFG14	29.5	16.0	75	1.0	1.00	1.4E+19	6.7
ITCS087	NN	16.6	10.7	70	1.0	6.2	TFG15	18.6	11.6	75	1.0	0.55	3.5E+18	6.3
ITCS089	RL	21.7	8.7	80	12.0	6.3	TFG18	21.7	8.7	75	10.0	0.62	3.5E+18	6.3